Title
Observation and analysis of Fano-like lineshapes in the Raman spectra of molecules adsorbed at metal interfaces

Journal
Physical Review B, 93(3)

ISSN
2469-9950

Authors
Dey, S
Banik, M
Hulkko, E
et al.

Publication Date
2016

DOI
10.1103/physrevb.93.035411

Observation and analysis of Fano-like lineshapes in the Raman spectra of molecules adsorbed at metal interfaces

S. Dey,[1] M. Banik,[1] E. Hulkko,[1,2] K. Rodriguez,[1] V. A. Apkarian,[1] M. Galperin,[3] and A. Nitzan[4,5]

[1]*Department of Chemistry, University of California, Irvine, California 92697-2025, USA*
[2]*Depratment of Chemistry, PO Box 35, FI-40014, University of Jyväskylä, Finland*
[3]*Department of Chemistry and Biochemistry, University of California at San Diego, La Jolla, CA 92093, USA*
[4]*Department of Chemistry, University of Pennsylvania, Philadelphia, Pennsylvania 19104, USA*
[5]*School of Chemistry, Tel Aviv University, Tel Aviv, 69978, Israel*

Surface enhanced Raman spectra from molecules (bipyridyl ethylene) adsorbed on gold dumbells are observed to become increasingly asymmetric (Fano-like) at higher incident light intensity. The electronic temperature (inferred from the anti-Stokes (AS) electronic Raman signal increases at the same time while no vibrational AS scattering is seen. These observations are analyzed by assuming that the molecule-metal coupling contains an intensity dependent contribution (resulting from light-induced charge transfer transitions as well as renormalization of the molecule metal tunneling barrier). We find that interference between vibrational and electronic inelastic scattering routes is possible in the presence of strong enough electron-vibrational coupling and can in principle lead to the observed Fano-like feature in the Raman scattering profile. However the best fit to the observed results, including the dependence on incident light intensity and the associated thermal response is obtained from a model that disregards this coupling and accounts for the structure of the continuous electronic component of the Raman scattering signal. The temperatures inferred from the Raman signal are argued to be only of qualitative value.

PACS numbers: 85.65.+h 73.23.-b 78.20.Jq 78.67.-n

Surface enhanced optical response of molecules adsorbed on metal surfaces reflects the effect of strong local fields created by surface plasmons[1–3] as well as charge transfer between the molecule and metal.[4–7] Surface enhanced Raman scattering (SERS) has become an important diagnostic tool for molecules at metallic interfaces including molecular conduction junctions.[8–15] (See also Refs. 16–25 for related theoretical work). At metal interfaces, vibrational Raman scattering is accompanied by a continuous background resulting from inelastic contributions of electron-hole (e-h) excitations in the metal.[1, 4, 26–28] Both components of the inelastic scattering signal were recently used to determine the bias induced heating in a molecular conduction junction.[13]

While it is generally recognized that the electronic background is affected by the molecule-substrate interaction, these two components of the SERS signal are usually treated separately. Surprizingly, we observe (Fig. S1) an apparent Fano-like feature that may indicate interference between these two scattering channels. Below we discuss the origin of this observation.

The measurements are carried out on single silica encapsulated gold dumbbells (Fig. S1 right inset). The nanosphere diameter is 95 ± 5 nm and the intersphere spacing prior to irradiation is $\sim$ 1 nm. On these dumbbells, the quadrupolar and the binding dipolar plasmon resonances occur near 560 nm and 780 nm, respectively.[29] As molecular reporter, bipyridyl ethylene (BPE) is adsorbed on the gold spheres prior to encapsulation. The dumbbells are dispersed on a silicon nitride membrane (20 nm thick) of the TEM grid by drop casting them in a dilute solution. Locations and geometries of the nanostructures are mapped using a scanning electron microscope (SEM), then Raman scattering measurements are done under an optical microscope, in the backscattering geometry, using an objective with a numerical aperture of NA = 0.625. The excitation source is a continuous wave diode laser, operating at λ = 532 nm, coincident with the anti-bonding quadrupolar surface plasmon resonance.[29] The molecular vibrational Raman spectra appear over a background continuum (Fig. S1b), which is also seen on bare dumbbells (Fig. S1a). As discussed before,[30] at low intensity, 10 μW/μm^2, the vibrational spectrum matches that of the isolated BPE molecule. Two observations are most significant at higher incident intensity: (a) The molecular lines broaden asymmetrically to eventually coalesce into the single asymmetric profile, similar to Fano-type lineshape (Figs. S1c and d). (b) The electronic and vibrational temperatures, T_e and T_v, inferred from the AS branch of the electronic Raman scattering and S/AS intensity ratio of the vibrational Raman line appear to be different. At the highest incident light intensity T_e reached 580 K, while no molecular AS scattering is seen, which would set the apparent vibrational temperature of the molecule, T_v, to less than 300 K. More experimental details and results are presented in the SI.

The central question raised by these observations is whether the lineshapes shown in Figs. S1c, d are indeed interference features as their Fano-like lineshapes suggest. Specifically: can there be interference between the electronic and vibrational Raman scattering pathways that coexist in this system? The intuitive answer is negative, because the two pathways lead to different final

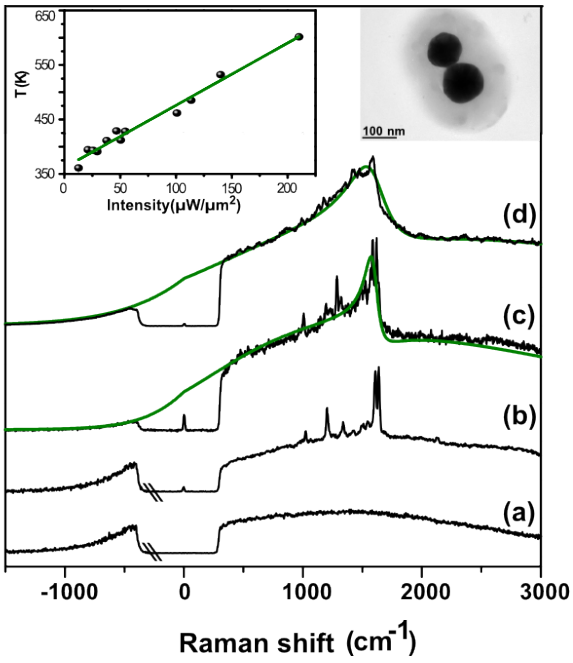

FIG. 1: Raman spectrum recorded on (a) a bare dumbbell, without reporter molecules at low irradiation intensity ($\sim 10\ \mu\mathrm{W}/\mu\mathrm{m}^2$); (b) with reporter molecules at the same low intensity; (c) and (d) with reporter molecules at irradiation intensities $\sim 50\ \mu\mathrm{W}/\mu\mathrm{m}^2$ and $\sim 150\ \mu\mathrm{W}/\mu\mathrm{m}^2$, respectively. Demarcations on (a) and (b) indicate a magnification of the anti-Stokes (AS) region (7x and 4.5x, respectively). The green traces overlapping the (c) and (d) lines are fits to the Fano lineshape (see SI). The right inset shows a TEM image of a typical dumbbell. The left inset shows the temperature extracted from the fit of the AS branch of the electronic Raman spectrum (continuum) to the Fermi Dirac distribution. No vibrational AS signal is detected.

states. The model calculations presented below yield two main results: (a) The aforementioned interference can exist and can in principle lead to the observed lineshapes. (b) However, comparing the detailed calculations with the available experimental observations suggests that another mechanism, asymmetric electronic sidebands dressing the molecular Raman spectrum, may be dominant.

We consider a molecule chemisorbed on a metal surface and subjected to an external radiation field. In the experimental system the metal is a nanostructure (NS) that promotes plasmonic enhancement, but this enters our discussion only implicitly, through the magnitude of the local electromagnetic field. The model Hamiltonian comprises the molecule, metal, radiation field and their couplings, with the electron-photon and e-v interaction terms treated as perturbations:

$$\hat{H} = \hat{H}_0 + \hat{V}_{rad} + \hat{V}_{e-v} \tag{1}$$

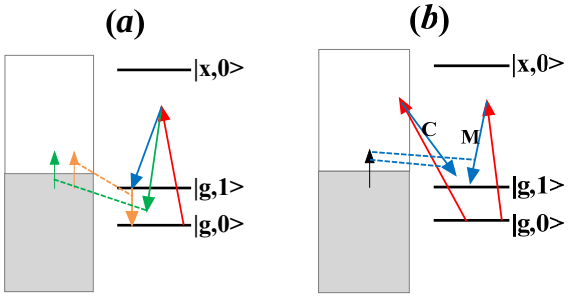

FIG. 2: (Color online) A sketch of the processes underlying the Stokes (S) component of Raman scattering from a molecule coupled to a metal. (a) The incident photons induce the virtual transition displayed in red and a corresponding Rayleigh scattering (the red process in reverse). In addition two inelastic scattering (Raman) pathways are shown: The green process brings the molecule back to its ground state while creating an e-h excitation in the metal (electronic Raman scattering). The blue process brings the molecule to an excited vibrational state on the electronic ground state (vibrational Raman scattering). These Raman scattering pathways are coupled by the combined effect of the metal-molecule electron- transfer coupling and the electronic-vibrational (e-v) interaction (orange) that induces vibrational de- excitation in the molecule with e-h formation in the metal. The dashed lines connect coupled processes. (b) Two pathways are defined by the excitation process (red): A (virtual) molecular transition and a molecule-to-metal charge transfer transition, respectively denoted M and C in the text. The outgoing photon (blue) leaves the molecule in the excited vibrational state, possibly with e-h excitation (or de- excitation) in the metal (black). Note that the processes shown are accompanied also by electronic Raman scattering from the bare metal.

where ($\hbar = k_B = e = 1$)

$$\hat{H}_0 = \hat{H}_M + \hat{H}_{NS} + \hat{V}_{NS} + \hat{H}_{rad}; \tag{2}$$

$$\hat{H}_M = \sum_{m=g,x} \varepsilon_m \hat{d}_m^\dagger \hat{d}_m + \omega_v \hat{v}^\dagger \hat{v}; \tag{3}$$

$$\hat{H}_{NS} = \sum_k \varepsilon_k \hat{c}_k^\dagger \hat{c}_k; \tag{4}$$

$$\hat{V}_{NS} = \sum_{m=g,x} \sum_k \left(V_{mk} \hat{d}_m^\dagger \hat{c}_k + V_{km} \hat{c}_k^\dagger \hat{d}_m \right); \tag{5}$$

$$\hat{V}_{e-v} = \sum_{m=g,x} M_m \hat{Q}_v \hat{d}_m^\dagger \hat{d}_m; \hat{Q}_v = \hat{v} + \hat{v}^\dagger \tag{6}$$

$$\hat{H}_{rad} = \sum_{\alpha \in i,\{f\}} \nu_\alpha \hat{a}_\alpha^\dagger \hat{a}_\alpha; \tag{7}$$

$$\hat{V}_{rad} = \hat{V}_{rad}^C + \hat{V}_{rad}^M \tag{8}$$

$$= \sum_{J=C,M} \sum_{\alpha \in i,\{f\}} \left(U_{gx,\alpha}^J(\hat{Q}_v)\, \hat{D}_J^\dagger \hat{a}_\alpha + U_{\alpha,gx}^J(\hat{Q}_v)\, \hat{a}_\alpha^\dagger \hat{D}_J \right)$$

$\hat{H}_M$ is the molecular Hamiltonian, modeled as a two electronic levels (ground and excited states, g and x) system with a single molecular vibration of frequency ω_v. $\hat{V}_{e-v}$ is the corresponding polaronic-type e-v coupling. $\hat{H}_{NS}$

describes a free electron metal and $\hat{V}_{NS}$ is the molecule-metal electron transfer coupling. $\hat{d}_m^\dagger$ ($\hat{d}_m$) (m=g, x) and $\hat{c}_k^\dagger$ ($\hat{c}_k$) create (annihilate) electrons in the molecular orbitals and the metal, respectively. $\hat{v}^\dagger$ ($\hat{v}$) and$\hat{a}_\alpha^\dagger$ ($\hat{a}_\alpha$) create (annihilate) vibrational excitations and photons in mode α, respectively. Finally, $\hat{D}_M = \hat{d}_g^\dagger \hat{d}_x$ and $\hat{D}_C = \hat{d}_g^\dagger \hat{c}_k$ are respectively intramolecular and charge-transfer electronic de-excitation operators. $\hat{V}_{rad}$, Eq. (8), is the system-radiation field coupling in which the coupling matrix elements $U^J_{gx,\alpha}$ connect the molecular ground state g to excited states x in the channels $J = C$ or M that determines the nature of the excited states x (a similar term, not shown, is associated with light scattering from the bare metal). As usual we distinguish between the incoming (occupied) photon mode i and the continuum of accepting (empty) modes $\{f\}$. These coupling elements are assumed to be functions of the vibrational coordinate, described here by their Taylor expansion up to linear term ($J = M, C$)

$$U^J_{gx,\alpha}(\hat{Q}_v) \equiv U^{J*}_{\alpha,gx}(\hat{Q}_v) \approx U^{J0}_{gx,\alpha} + U^{J1}_{gx,\alpha}\hat{Q}_v \tag{9}$$

To account for the observed dependence of the inelastic spectrum on the incident light intensity, we assume that in addition to being scattered, the incident radiation field affects the molecule-metal coupling. This can arise from a field-induced renormalization of the electron transfer coupling $\hat{V}_{NS}$, Eq. (5),[31–33] as well as contributions from molecule to metal charge transfer transitions. In the calculations reported below this is incorporated by an assumed dependence of the self-energies Γ_m ($m = g, x$) on the incident light intensity.

Consider first model A (Fig. S2a). Here we assume that Raman scattering is dominated by the intramolecular optical transition and disregard the corresponding contribution of the optical charge transfer coupling V^C_{rad}. This model can show interference between the vibrational and electronic scattering channels, provided that their coupling, Eq (6), is strong enough.

Following the procedure described in Ref. 18 the (normal) Raman scattering flux [43] has the following structure

$$\begin{aligned} J_{i\to f} = &\int_{-\infty}^{+\infty} d(t'-t) \int_{-\infty}^{0} d(t_1-t) \int_{-\infty}^{0} d(t_2-t') \\ &\times e^{-i\nu_f(t'-t)}\, e^{-i\nu_i(t_1-t_2)} \\ &\times \left\langle \hat{U}_i(t_2)\hat{D}(t_2)\hat{U}_f(t')\hat{D}^\dagger(t')\hat{U}_f(t)\hat{D}(t)\hat{U}_i(t_1)\hat{D}^\dagger(t_1)\right\rangle \end{aligned} \tag{10}$$

in which the operators are summed over all relevant contributions from Eqs. (8) and (9) and where the indices i and f indicate that the corresponding matrix element should be taken with the incident or scattered radiation field modes, respectively. In departure from Ref. [18] we keep only the lowest order (up to 2^{nd}) terms in U^1, as usually done for non-resonant Raman calculations. The calculation proceeds as follows (See the SI for details):

(a) Applying Eq. (S2) to model A, yields Eqs. (S2) for the light scattering flux. Analysis based on energy conservation suggests that expressions (S2a), (S2f) and (S2k) contribute to Rayleigh and pure electronic Raman scattering, while expressions (S2g) - (S2j) contribute to vibrational Raman scattering (possibly dressed by e-h excitations).[44] Expressions (S2b) - (S2e) formally represent interference between vibrational and electronic-Raman/Rayleigh scattering. At the level of the present calculation, fourth order in the coupling to radiation field, they vanish in the absence of the coupling(6).

(b) The e-v interaction (6) is considered to the lowest order. This introduces an additional term

$$\int_c d\tau_v\, M_g\, \hat{Q}_v(\tau_v)\, \hat{n}_g(\tau_v) \tag{11}$$

into the correlation functions (S2b)-(S2e), yielding non-vanishing corrections that represent interference between the electronic and vibrational Raman processes that can give rise to Fano lineshape in the Raman scattering as shown below.[45] In evaluating these terms, the real time analog, t_v, of the contour variable τ_v can be placed in all possible ways between the times t, t', t_1, and t_2 on the Keldysh contour (see Fig. S5).

(c) The light scattering flux including the interference corrections is thus obtained in terms of correlation functions of a system defined by the quadratic Hamiltonian H_0. Thus Wick's theorem applies and electronic and vibrational degrees of freedom decouple yielding the final expressions in terms of projections to real time of the electronic and vibrational Green functions, $G_{mm'}(\tau,\tau') \equiv -i\langle T_c\, \hat{d}_m(\tau)\, \hat{d}^\dagger_{m'}(\tau')\rangle$ and $D(\tau,\tau') \equiv -i\langle T_c\, \hat{Q}_v(\tau)\, \hat{Q}_v(\tau')\rangle$, where T_c is the contour ordering operator. For the molecular vibration we use the quasiparticle approximation, Eqs. (S3) and (S4). In evaluating the electronic GFs we assume $\varepsilon_x - \varepsilon_g \gg \Gamma_m$, where $\Gamma_m = 2\pi \sum_k |V_{km}|^2 \delta(E - \varepsilon_k)$; $m = g, x$. Consequently, interstate correlations induced by the metal are neglected, $G_{mm'}(\tau,\tau') \approx \delta_{m,m'} G_{mm}(\tau,\tau') \equiv \delta_{m,m'} G_m(\tau,\tau')$, leading to the standard expressions (S5)-(S7) for the electronic GFs.

This procedure leads to explicit expressions, Eqs. (S8)-(S14), for the different contributions to the light scattering flux in the relevant order (fourth) in the system-radiation field coupling including the interference corrections, Eqs. (S10) and (S14), arising from the e-v coupling. The other contributions can be classified according to their physical origin that can be identified by their energy conservation structure. Eq. (S8d) and (S10d) represent the the Rayleigh scattering component that is disregarded in our calculation. Eq. (S8) represents the pure electronic Raman that may be though of as an electronic sideband of the Rayleigh peak.[46] We have previously[34, 35] used the Stokes (S) and anti-Stokes (AS) components of this contribution to estimate the apparent electronic heating in non-equilibrium molecu-

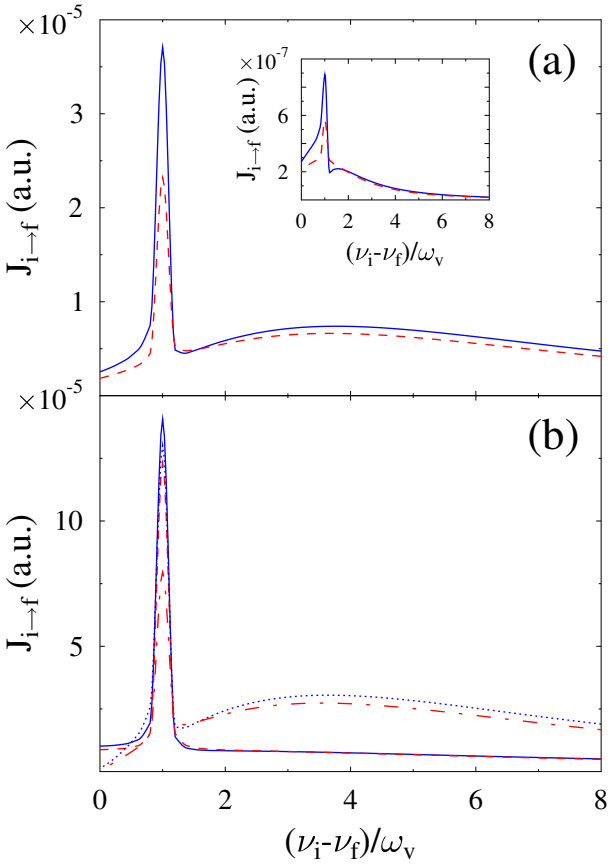

FIG. 3: (Color online) (a) The total Raman scattering (full line; blue) evaluated from Eqs. (S8)-(S14) (without the Rayleigh contributions, Eqs. (S8d) and (S10d)), displayed against the Raman shift $\nu_i - \nu_f$. The parameters used are $T = 300$ K, $\varepsilon_g = 0$, $\varepsilon_x = 2$ eV, $\Gamma_g = \Gamma_x = 0.05 + \Gamma^{opt}$ eV with $\Gamma^{opt} = 0.3$ eV being the light induced tunneling rate, $\omega_v = 0.05$ eV, $M_g = 0.02$ eV, $\nu_i = 1$ eV, $U^{(0)} = 0.1$ eV, $U^{(1)} = 0.01$ eV. The red dashed line is the result obtained when the e-v interaction (6) is disregarded. The inset shows the corresponding weak incident field case with $\Gamma^{opt} = 0.03$ eV, $U^{(0)} = 0.032$ eV, $U^{(1)} = 0.0032$ eV. (b) The Raman scattering calculated with the same parameters as in the main panel on the left at temperatures 3000 K (solid and dashed lines) and 30 K (dotted and dash-dotted lines, multiplied by a scale-factor 4).

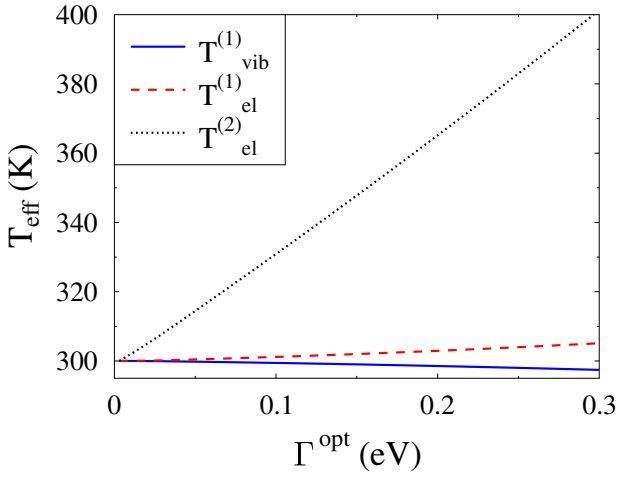

FIG. 4: The effective temperature obtained from the Raman scattering spectrum displayed in the main panel of Fig. 3. See text for details.

lar junctions. Eq. (S13) is the vibrational contribution to the Raman signal together with its own electronic sideband.

Fig. S3 shows the total Raman scattering signal resulting from this model calculation. The calculation was done on an energy grid spanning the region from -3 to 3 eV with step 10^{-3} eV and the molecular vibration is assumed to equilibrate quickly to the ambient temperature. The following observations can be made:

(a) Interference between electronic and vibrational inelastic scattering routes can indeed lead to a Fano-type scattering spectrum. The electron-vibration coupling (6) is crucial for obtaining this behavior. This is seen in the weak illumination case (inset to Fig. S3a) by comparing the results obtained with and without this coupling.

(b) The asymmetric lineshape that seen in the high incident intensity case (main figure S3a) is not of this origin. In this case the calculation yields Fano-like lineshapes that qualitatively reproduce the experimental behavior also when the coupling (6) is disregarded.

(c) The transition from a standard, essentially symmetric Raman line to a broadened assymetric line when the incident light intensity increases is best rationalized within this model by assuming that the coupling (6) is small enough to be disregarded. This yields the dashed lines in Figure S3 that qualitatively agree with the experimental observation.

Our analysis thus shows that interference between vibrational and electronic Raman scattering can in principle occur leading to a characteristic Fano lineshape in Raman scattering from molecules adsorbed on metal substrates. It suggests, however, that the origin of of the present observation of asymmetric Raman lineshape at higher (photoinduced) metal-molecule coupling is different resulting from the S component of the electronic Raman scattering. This is seen in the Fig. S3b, that show that the asymmetry disappears at high ambient temperatures.

Our calculation also yields the effective (Raman) temperature from the ratio between the S and AS scattering intensities according to [13, 17, 18] $T^{(1)}_{eff} = \frac{\Delta\nu}{\ln\left(J_{\nu_i\to\nu_i-\Delta\nu}/J_{\nu_i\to\nu_i+\Delta\nu}\right)}$, or fitting the tail of the AS signal to $a\,\Delta\nu/\left(1-\exp[-\Delta\nu/T^{(2)}_{eff}]\right)$, Eq.(S1), where $\Delta\nu \equiv |\nu_i - \nu_f|$ is the Raman shift. For $T^{(1)}_{eff}$ we have arbitrarily assigned the vibrational Raman temperature to the value calculated at $\Delta\nu = \omega_v$ and the electronic Ra-

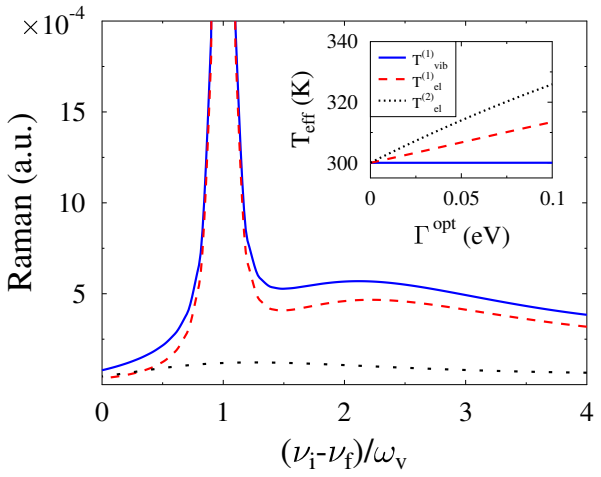

FIG. 5: The Raman scattering signal calculated for model B (see text for parameters). The dotted-black and dashed-red lines represent the signals associated with the pure-electronic and electronic-dressed vibrational Raman, respectively, and the full blue line is their sum. The inset shows the corresponding vibrational and electronic effective temperatures, calculated as before.

man temperature to that obtained at $\Delta\nu = 2\omega_v$. The results for the parameters of Fig. S3a (main panel) are shown in Fig. S4. The resulting trends are similar to those observed experimentally, although the model calculation somewhat underestimates the electronic heating. In spite of this qualitative agreement with the experimental observation, we note that while T_{eff} can give a rough estimate of system heating, the actual numbers may be meaningless. This is indicated here by discrepancy between the different calculations of T_{el} and the apparent cooling seen in T_{vib}, keeping in mind that the oscillator was kept at the ambient temperature in this calculation.

We have also considered model B as an alternative mechanism for interference. The calculation follows the same steps as in (a) and (c) above, now using both M and C terms in Eq. (8) and again keeping only terms up to the lowest order in U^1 (Eq. (9)). In this calculation we have restricted our considerations to contributions from the purely intra-molecular processes ($\hat{D} = \hat{D}_M$ in all four terms in (S2)), purely charge-transfer processes ($\hat{D} = \hat{D}_C$ in all terms), and their mixtures (potential source of interference) in which excitation operators at times t_2 and t' are of one kind, while those at times t and t_1 of the other. Again the molecule-metal tunneling coupling Γ_m is assumed to contain an incident field dependent contribution.[47] The final result for the light scattering flux for this model is given by Eqs. (S15)-(S19).

Fig. S5 shows the Stokes side of the Raman response obtained from this model using the following parameters: $T = 300$ K, $\varepsilon_g = 0$ eV, $\varepsilon_x = 2$ eV, $\omega_v = 0.1$ eV, $\nu_i = 1$ eV, $\Gamma_g = \Gamma_x = 0.15$ eV $+ \Gamma^{opt}$ with $\Gamma^{opt} = 0.1$ eV, $U^{(0)}_{M\alpha} = 0.1$ eV and $U^{(1)}_{M\alpha} = 0.01$ eV ($\alpha = i, f$), and $E_F = 0$. Calculations are performed on an energy grid spanning the region from -5 to 5 eV with step 10^{-3} eV. Asymmetric Raman profiles are seen as before, but again we find (see SI) that while there is some contribution of interference between channels M and C, the main source of lineshape asymmetry originates again from the electronic sideband that dresses the Rayleigh and vibrational scattering peaks mainly on their blue side. The "electronic heating" obtained here is stronger than in model A, closer to the magnitude observed experimentally, but the actual numbers should again be considered cautiously.

In conclusion, we have observed asymmetric lineshape features in Raman scattering from bipyridyl ethylene molecules adsorbed on gold nanostructures, with the following characteristics: (a) Asymmetry increases with incident light intensity. (b) The vibrational temperature appears not to increase even at the highest intensity used, while the apparent electronic temperature increases by up to ~ 600 K. The Fano-like appearance of these lineshapes suggests the possibly implication of interference between different scattering pathways. Model calculations show that such interference, leading to the observed asymmetry, is indeed possible in systems with strong enough electron-vibrational coupling. Our calculations suggest, however, that the observed lineshape asymmetry is dominated by electronic scattering sidebands that dress the Rayleigh and vibrational scattering peaks, and its dependence on incident light intensity can be explained by an optically induced component in the molecule-metal electron-transfer coupling. This model also yields vibrational and electronic "Raman temperatures" that are consistent with experimental observation, but may reflect the complex nature of the non-equlibrium response rather than the actual temperature. Fano-type interference in Raman scattering has been shown to be a theoretical possibility.

The Research of AN is supported by the Israel Science Foundation and by the US-Israel Binational Science Foundation. AN thanks the Theoretical Physics Group at the Free University of Berlin for hospitality. MG gratefully acknowledges support by the DOE (Early Career Award, de-sc0006422). The experimental work was carried out at the NSF Center for Chemistry at the Space-Time Limit (CHE-0802913). EH is supported by the Academy of Finland (Decision No. 265502).

SUPPLEMENTARY INFORMATION

Experimental Details

s outlined in the main text, the measurements are carried out on single silica encapsulated gold dumbbells, the transmission electron micrograph (TEM) of which is shown in the inset to Fig. S1. The nanosphere diameter is 95±5 nm and the intersphere spacing prior to irradiation is $\sim$ 1 nm. As molecular reporter, bipyridyl ethylene (BPE) is adsorbed on the gold spheres prior to encapsulation. The dumbbells are dispersed on a silicon nitride membrane (20 nm thick) of the TEM grid by drop casting them in a dilute solution. After mapping out locations and geometries of the nanostructures using a scanning electron microscope (SEM), Raman scattering measurements are carried out under an optical microscope, in the backscattering geometry, using an NA = 0.625 objective. The excitation source is a continuous wave diode laser, operating at $\lambda = 532$ nm, which is resonant with the anti-bonding quadrupolar plasmon on these structures.[29, 36] On these dumbbells, the binding quadrupolar plasmon and the binding dipolar plasmon resonances occur near 560 nm and 780 nm, respectively.[29] The molecular vibrational Raman spectra invariably appear over a background continuum (Fig. S1b), which can also be seen on bare dumbbells (Fig. 1a). The molecular lines broaden asymmetrically as a function of irradiation intensity, to eventually coalesce into the asymmetric Fano-like profile shown in Fig. S1c and 1d. We see variations in details on different particles, along with hysteretic response during intensity cycling due to evolution in the structure of the intersphere junction, which is verified through TEM. A rich variety of phenomena can be identified during fusion of the plasmonic junction when the incident light intensity increases.[36] Here, we focus on the development of the Fano-like profile that possibly indicates interference between the electronic Raman scattering continuum on gold and the discrete resonances of the molecule. The temperature of the molecular vibrations is inferred from the usual ratio of Stokes/Anti-Stokes scattering. The electronic temperature is obtained from the anti-Stokes branch of the continuum, which for Raman shifts $\mathcal{E} = \omega_i - \omega_s > kT$, can be seen in Fig. S2 to decay exponentially, $\exp(-\mathcal{E}/kT_e)$, as expected for e-h Raman scattering that terminates on thermally populated holes. The spectrum is explicitly fitted to the joint density of states, which appears in first term of Eq. (S1). The principal experimental observations are summarized as follows:

1. At low intensity, $10\mu\mathrm{W}/\mu\mathrm{m}^2$, the molecular vibrational Raman spectrum that appears over the background continuum in Fig. S1b, perfectly matches that of the isolated BPE molecule. Note that the traces in Fig. S1 are identical to those in Fig. 1 of the main text. This has been shown in some detail previously.[30]

2. The background continuum, which is also present on the bare dumbbell (Fig. S1a), can be assigned to electronic Raman scattering (ERS) on the gold nano antenna. The continuum is polarized. As in the Hertzian antenna,[37] the scattering is dipolar, with $cos^4 q$ polarization along the long axis of the dumbbell.

3. The fits of the anti-Stokes spectra to Eq. S1), which are shown in Fig. S2, yield the effective electronic temperature of the gold. This has been independently recognized recently.[38] Note, the method does not involve a ratio between Stokes and anti-Stokes scattering, which can be misleading. T_e, is a linear function of the irradiation intensity, as seen in Fig. S3a.

4. As the excitation intensity is increased up to 400 $\mu\mathrm{W}/\mu\mathrm{m}^2$, the molecular lines develop asymmetric profiles and gain intensity relative to the background. At high intensity, the molecular response collapses into a single asymmetric line. The spectral profiles S1c and S1d can be fitted to a sum of ERS background and a Fano line, according to

$$W(\mathcal{E}) = a\int f(E)\left(1 - f(E+\mathcal{E})\right)e^{-|2\mathcal{E}/\mathrm{d}|}dE + b\left[\frac{(q+\epsilon)^2}{1+\epsilon^2} - 1\right] \tag{S1}$$

   in which *a,b* are normalization constants *(a/b* =20), *f(E)* is the Fermi-Dirac distribution, $d = 0.19$ eV is the energy width of the projection of the collective plasmon state on single particle states,[39] $\epsilon = \frac{(\mathcal{E}-\omega_0)}{\gamma/2}$ is the reduced frequency with center on the molecular vibrational frequency, w_0= 1600 cm^{-1}. The resulting fits are shown as green traces overlapping the lines c and d in Fig. S1. In Fig. S1c the fit parameters are $\gamma = 130$ cm^{-1} and $q = 2.5$, while in Fig. S1d $\gamma = 390$ cm^{-1} and $q = 2.7$.

5. While the ERS background shows linear dependence on irradiation intensity, the integrated area under the molecular lines is superlinear, as shown in Fig. S3b.

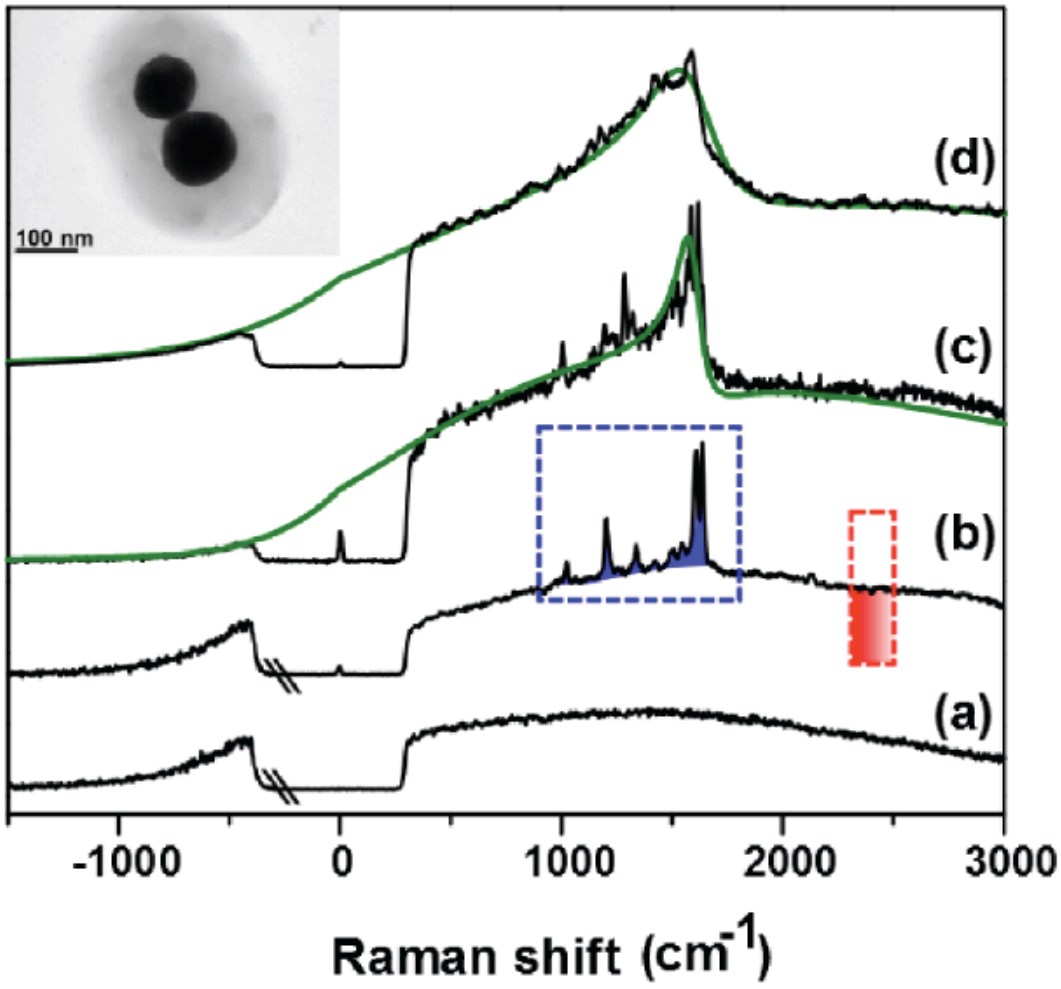

FIG. S1: (a) Raman spectrum recorded on a bare dumbbell, where reporter molecules are absent at the metallic junction. (b) Molecular Raman lines of BPE appear over the background continuum from a dumbbell. Both (a) and (b) have been recorded at low intensity ($\sim 10\mu\mathrm{W}/\mu\mathrm{m}^2$) and anti-Stokes region is expanded vertically for clarity in either case (7x and 4.5x, respectively). At elevated irradiation intensity the entire spectrum develops Fano-like profile. Parentage of the molecular lines may still be identified (c) at moderate intensity ($\sim 50\mu\mathrm{W}/\mu\mathrm{m}^2$) and becomes unidentifiable (d) at more intense irradiation ($\sim 150\mu\mathrm{W}/\mu\mathrm{m}^2$). The entire line profile in (c) and (d) can be fitted to Fano lineshape (green trace). The inset shows a TEM image of a typical dumbbell. Shaded regions are used to quantify the intensity dependence of molecular lines (blue) and electronic Raman scattering of gold (red), the results of which are shown in Fig. S1b.

6. Remarkably, the molecular vibrations and metal electrons appear to have different temperatures. At the highest incident light intensity, where the apparent electron temperature reaches $T_e = 580$ K, we see no evidence of molecular anti-Stokes scattering. Based on the Stokes to anti-Stokes ratio, we establish that the apparent vibrational temperature of the molecule, T_v, is less than 300 K.

7. Near 1 $\mathrm{mW}/\mu\mathrm{m}^2$, the nano-structure undergoes phase explosion – the metal melts and the silica shell explodes. Hysteretic behavior is observed during intensity cycling at intensities in excess of $\sim 100\mu\mathrm{W}/\mu\mathrm{m}^2$, due to permanent evolution of the junction structure. The spectrum in Fig. S1c, which was recorded at an irradiation intensity of $50\mu\mathrm{W}/\mu\mathrm{m}^2$, was obtained after such a cycle.

Theoretical Details

Here we present details on derivation of Raman signal expressions for the two models considered in the paper. The starting point is general expression of the normal Raman scattering (see Eq.(9) of the paper and Fig. S4 below)

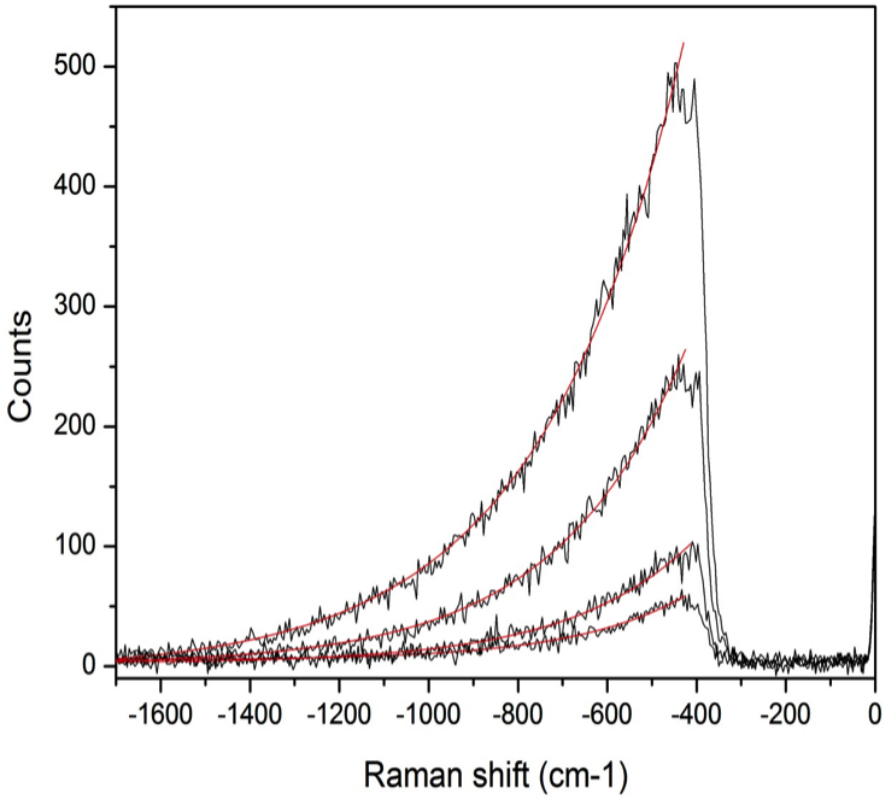

FIG. S2: The anti-Stokes branch of the continuum is given by the thermal occupation of the Fermi-Dirac distribution. This is illustrated by the exponential fits, $I_{AS}(\mathcal{E}) = \exp(-\mathcal{E}/kT_e)$, to the anti-Stokes continuum for four different irradiation intensities, $I = 100, 50, 25, 13\mu\text{W}/\mu\text{m}^2$, which yield electronic temperatures of $T_e = 465, 415, 395, 364$ K, respectively. A more accurate value of T_e is obtained from fitting to (S1), but the trend does not change.

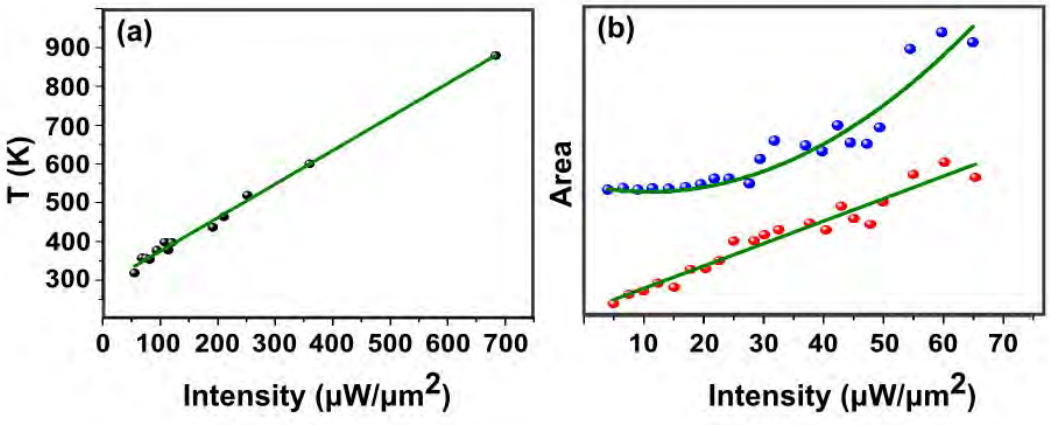

FIG. S3: (a) Exponentially decaying anti-Stokes branch of Raman spectra determines the temperature at the metallic junction which grows linearly with increasing irradiation intensity. (b) The electronic Raman scattering background (red dot) varies linearly with irradiation intensity. However, the area under the molecular lines (blue dot) is superlinear.

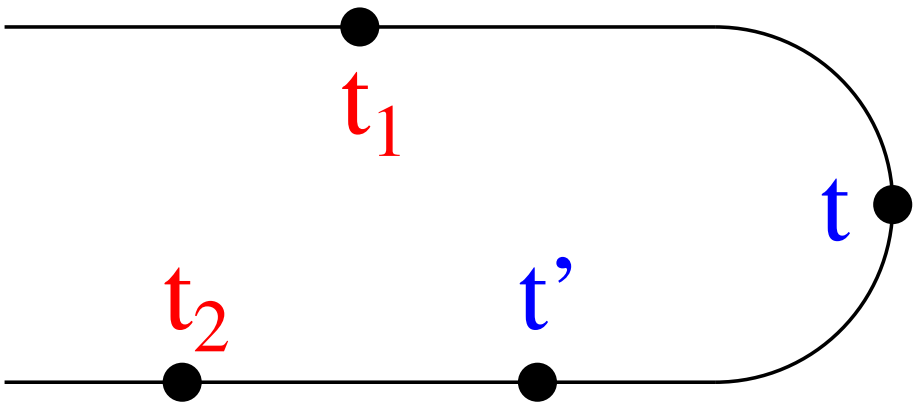

FIG. S4: (Color online) Projection for 'the normal Raman' scattering. Times t_1 and t_2 indicate interaction with the incoming photon ν_i, t and t' - with the outgoing photon ν_f. The diagram is identical to Fig. 8a of Ref. [18].

[18, 40, 41].

Utilizing Taylor expansion of the optical electronic transition matrix element (see Eq.(8) of the paper) and keeping terms up to second order in molecular vibration coordinate leads to the following steady-state expression for Raman scattering from mode i to mode f of the radiation field

$$J_{i\to f} = \int_{-\infty}^{+\infty} d(t'-t) \int_{-\infty}^{0} d(t_1-t) \int_{-\infty}^{0} d(t_2-t')\, e^{i\nu_f(t-t')} - i\nu_i(t_1-t_2)$$

$$\Big[U^{(0)}_{i,gx}U^{(0)}_{gx,f}U^{(0)}_{f,gx}U^{(0)}_{gx,i}\langle\hat{D}(t_2)\hat{Q}_v(t_2)\,\hat{D}^\dagger(t')\,\hat{D}(t)\,\hat{D}^\dagger(t_1)\rangle \tag{S2a}$$

$$+ U^{(1)}_{i,gx}U^{(0)}_{gx,f}U^{(0)}_{f,gx}U^{(0)}_{gx,i}\langle\hat{D}(t_2)\hat{Q}_v(t_2)\,\hat{D}^\dagger(t')\,\hat{D}(t)\,\hat{D}^\dagger(t_1)\rangle \tag{S2b}$$

$$+ U^{(0)}_{i,gx}U^{(1)}_{gx,f}U^{(0)}_{f,gx}U^{(0)}_{gx,i}\langle\hat{D}(t_2)\,\hat{D}^\dagger(t')\hat{Q}^\dagger_v(t')\,\hat{D}(t)\,\hat{D}^\dagger(t_1)\rangle \tag{S2c}$$

$$+ U^{(0)}_{i,gx}U^{(0)}_{gx,f}U^{(1)}_{f,gx}U^{(0)}_{gx,i}\langle\hat{D}(t_2)\,\hat{D}^\dagger(t')\,\hat{D}(t)\hat{Q}_v(t)\,\hat{D}^\dagger(t_1)\rangle \tag{S2d}$$

$$+ U^{(0)}_{i,gx}U^{(0)}_{gx,f}U^{(0)}_{f,gx}U^{(1)}_{gx,i}\langle\hat{D}(t_2)\,\hat{D}^\dagger(t')\,\hat{D}(t)\,\hat{D}^\dagger(t_1)\hat{Q}^\dagger_v(t_1)\rangle \tag{S2e}$$

$$+ U^{(1)}_{i,gx}U^{(1)}_{gx,f}U^{(0)}_{f,gx}U^{(0)}_{gx,i}\langle\hat{D}(t_2)\hat{Q}_v(t_2)\,\hat{D}^\dagger(t')\hat{Q}^\dagger_v(t')\,\hat{D}(t)\,\hat{D}^\dagger(t_1)\rangle \tag{S2f}$$

$$+ U^{(1)}_{i,gx}U^{(0)}_{gx,f}U^{(1)}_{f,gx}U^{(0)}_{gx,i}\langle\hat{D}(t_2)\hat{Q}_v(t_2)\,\hat{D}^\dagger(t')\,\hat{D}(t)\hat{Q}_v(t)\,\hat{D}^\dagger(t_1)\rangle \tag{S2g}$$

$$+ U^{(1)}_{i,gx}U^{(0)}_{gx,f}U^{(0)}_{f,gx}U^{(1)}_{gx,i}\langle\hat{D}(t_2)\hat{Q}_v(t_2)\,\hat{D}^\dagger(t')\,\hat{D}(t)\,\hat{D}^\dagger(t_1)\hat{Q}^\dagger_v(t_1)\rangle \tag{S2h}$$

$$+ U^{(0)}_{i,gx}U^{(1)}_{gx,f}U^{(1)}_{f,gx}U^{(0)}_{gx,i}\langle\hat{D}(t_2)\,\hat{D}^\dagger(t')\hat{Q}^\dagger_v(t')\,\hat{D}(t)\hat{Q}_v(t)\,\hat{D}^\dagger(t_1)\rangle \tag{S2i}$$

$$+ U^{(0)}_{i,gx}U^{(1)}_{gx,f}U^{(0)}_{f,gx}U^{(1)}_{gx,i}\langle\hat{D}(t_2)\,\hat{D}^\dagger(t')\hat{Q}^\dagger_v(t')\,\hat{D}(t)\,\hat{D}^\dagger(t_1)\hat{Q}^\dagger_v(t_1)\rangle \tag{S2j}$$

$$+ U^{(0)}_{i,gx}U^{(0)}_{gx,f}U^{(1)}_{f,gx}U^{(1)}_{gx,i}\langle\hat{D}(t_2)\,\hat{D}^\dagger(t')\,\hat{D}(t)\hat{Q}_v(t)\,\hat{D}^\dagger(t_1)\hat{Q}^\dagger_v(t_1)\rangle\Big] \tag{S2k}$$

Analysis based on energy conservation suggests that from all the resulting diagrams expressions (S2a), (S2f) and (S2k) contribute to electronic Raman scattering (in particular, Eq. (S2a) leads to results discussed in out previous publications[34, 35]). Expressions (S2g)-(S2j) contribute to vibrational Raman scattering (these results are similar to those of resonant Raman scattering consideration in our previous publications[17, 18]). Finally, expressions (S2b)-(S2e) are responsible for interference between the electronic and vibrational intra-molecular Raman scattering channels (see details below), which is possible in the presence of electron-vibration interaction (see Eq.(5) of the paper). This situation is encountered in description of the model A (see Fig. 2a of the paper). If one disregards this interaction (and within the treatment of molecular coupling to radiation field up to second order in molecular vibration coordinate)

the latter contributions are zero. This is the situation encountered in description of the model B (see Fig. 2b of the paper). We now turn to details of derivation specific for each of the models.

Model A

Within this model we are interested in interference between electronic Raman scattering (a process where vibrational state at the start an end of Raman scattering is the same) and vibrational Raman scattering (a scattering process with initial and final states with different vibrational excitations) amplitudes. For the two amplitudes to interfere, final states of the two processes should be the same. Electron-vibration coupling in molecular Hamiltonian (see Eq.(5) of the paper), yields such a possibility (see Fig. 2a of the paper). In the off-resonant Raman regime electron-vibration interaction can be disregarded. Utilizing the first order perturbation in the electron-vibration coupling (see Eq.(10) of the paper) in expressions (S2b)-(S2e) results in the desired interference. Possible placements of the time of electron-vibration interaction t_v between times t, t' and t_1, t_2 representing interaction with the outgoing f and incoming i modes of the radiation field, respectively, are shown in Fig. S5.

Projections (e)-(h) of Fig. S5 utilized in corrections to (S2b)-(S2c) and projections (a)-(d) of Fig. S5 in corrections to (S2d)-(S2e) lead to renormalization of electronic Raman due to electron-vibration interaction. These are the diagrams which lead to Fano resonance in Raman scattering (see below). Projections (a)-(d) of Fig. S5 in corrections to (S2b)-(S2c) and projections (e)-(h) of Fig. S5 in corrections to (S2d)-(S2e) renormalize vibrational Raman scattering.

After accounting for the electron-vibration interaction we decouple electron and vibration degrees of freedom and utilize the Wick's theorem to get final expressions in terms of projections of electron and vibrational Green functions (see Eqs. (11) and (12) of the paper). We treat molecular vibration within quasiparticle approximation

$$D^{<}(\omega) = -2\pi i\left(N_v\delta(\omega-\omega_v)+[1+N_v]\delta(\omega+\omega_v)\right) \tag{S3}$$
$$D^{>}(\omega) = -2\pi i\left(N_v\delta(\omega+\omega_v)+[1+N_v]\delta(\omega-\omega_v)\right) \tag{S4}$$

where N_v is average population of the vibration. Explicit expressions for electronic Green functions are $(m=g,x)$

$$G^{<}_m(E) = \frac{i\Gamma_m f(E)}{(E-\varepsilon_m)^2+(\Gamma_m/2)^2} \tag{S5}$$
$$G^{>}_m(E) = \frac{-i\Gamma_m f(E)}{(E-\varepsilon_m)^2+(\Gamma_m/2)^2} \tag{S6}$$
$$G^{r}_m(E = [E-\varepsilon_m+i\Gamma_m/2]^{-1} \qquad G^{a}_m(E) = [G^{r}_m(E)]^* \tag{S7}$$

After tedious but straightforward algebra we get the following steady-state expressions for Raman scattering.

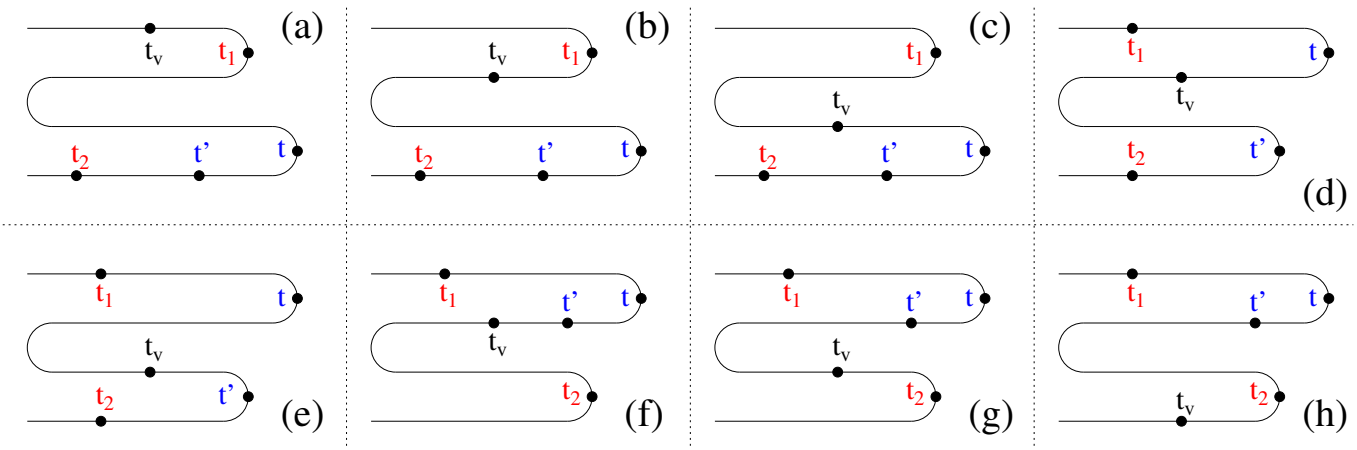

FIG. S5: (Color online) Electron-vibration interaction induced corrections to 'the normal Raman' (Fig. S4). t_v indicates time of interaction with molecular vibration. The contour is deformed following the Langreth rules [42].

Explicit expression for the electronic Raman is

$$\int \frac{dE_{g1}}{2\pi}\int \frac{dE_{g2}}{2\pi}\int \frac{dE_{x1}}{2\pi}\int \frac{dE_{x2}}{2\pi}\, 2\pi\delta(\nu_{if}-E_{g21}-E_{x21}) \tag{S8a}$$
$$G_g^<(E_{g1})G_g^>(E_{g2})G_x^<(E_{x1})G_x^>(E_{x2})\Bigg(\left|\frac{U^{(0)}_{f,gx}U^{(0)}_{gx,i}}{\nu_i-E_{x2}+E_{g1}+i\delta}\right|^2$$
$$+2\mathrm{Re}\,U^{(1)}_{i,gx}U^{(1)}_{gx,f}U^{(0)}_{f,gx}U^{(0)}_{gx,i}\Bigg[\frac{1+N_v}{(\nu_i-E_{x2g1}-\omega_v+i\delta)(\nu_i-E_{x2g1}-i\delta)}$$
$$+\frac{N_v}{(\nu_i-E_{x2g1}+\omega_v+i\delta)(\nu_i-E_{x2g1}-i\delta)}\Bigg]\Bigg)$$
$$+\int \frac{dE_{x1}}{2\pi}\int \frac{dE_{x2}}{2\pi}2\pi\delta(\nu_{if}-E_{x21})\,G_x^<(E_{x1})G_x^>(E_{x2}) \tag{S8b}$$
$$\Bigg(\left|\int \frac{dE_g}{2\pi}\frac{U^{(0)}_{f,gx}U^{(0)}_{gx,i}G_g^<(E_g)}{\nu_i-E_{x2}+E_g+i\delta}\right|^2-\int\frac{dE_{g1}}{2\pi}\int\frac{dE_{g2}}{2\pi}G_g^<(E_{g1})G_g^<(E_{g2})$$
$$\times 2\mathrm{Re}\,U^{(1)}_{i,gx}U^{(1)}_{gx,f}U^{(0)}_{f,gx}U^{(0)}_{gx,i}\Bigg[\frac{1+N_v}{(\nu_i-E_{x2g1}-\omega_v+i\delta)(\nu_i-E_{x2g2}-i\delta)}$$
$$+\frac{N_v}{(\nu_i-E_{x2g1}+\omega_v+i\delta)(\nu_i-E_{x2g2}-i\delta)}\Bigg]\Bigg)$$
$$+\int \frac{dE_{g1}}{2\pi}\int \frac{dE_{g2}}{2\pi}2\pi\delta(\nu_{if}-E_{g21})\,G_g^<(E_{g1})G_g^>(E_{g2}) \tag{S8c}$$
$$\Bigg(\left|\int \frac{dE_x}{2\pi}\frac{U^{(0)}_{f,gx}U^{(0)}_{gx,i}G_x^>(E_x)}{\nu_i-E_x+E_{g1}+i\delta}\right|^2-\int\frac{dE_{x1}}{2\pi}\int\frac{dE_{x2}}{2\pi}G_x^>(E_{x1})G_x^>(E_{x2})$$
$$\times 2\mathrm{Re}\,U^{(1)}_{i,gx}U^{(1)}_{gx,f}U^{(0)}_{f,gx}U^{(0)}_{gx,i}\Bigg[\frac{1+N_v}{(\nu_i-E_{x1g1}-\omega_v+i\delta)(\nu_i-E_{x2g1}-i\delta)}$$
$$+\frac{N_v}{(\nu_i-E_{x1g1}+\omega_v+i\delta)(\nu_i-E_{x2g1}-i\delta)}\Bigg]\Bigg)$$
$$+2\pi\delta(\nu_i-\nu_f)\Bigg(\left|\int\frac{dE_g}{2\pi}\int\frac{dE_x}{2\pi}\frac{U^{(0)}_{f,gx}U^{(0)}_{gx,i}G_g^<(E_g)G_x^>(E_x)}{\nu_i-E_x+E_g+i\delta}\right|^2 \tag{S8d}$$
$$+\int\frac{dE_{g1}}{2\pi}\int\frac{dE_{g2}}{2\pi}\int\frac{dE_{x1}}{2\pi}\int\frac{dE_{x2}}{2\pi}G_g^<(E_{g1})G_g^<(E_{g2})G_x^>(E_{x1})G_x^>(E_{x2})$$
$$\times 2\mathrm{Re}\,U^{(1)}_{i,gx}U^{(1)}_{gx,f}U^{(0)}_{f,gx}U^{(0)}_{gx,i}\Bigg[\frac{1+N_v}{(\nu_i-E_{x1g1}-\omega_v+i\delta)(\nu_i-E_{x2g2}-i\delta)}$$
$$+\frac{N_v}{(\nu_i-E_{x1g1}+\omega_v+i\delta)(\nu_i-E_{x2g2}-i\delta)}\Bigg]\Bigg)$$

Here

$$\nu_{if}\equiv\nu_i-\nu_f\quad E_{xm_xgm_g}\equiv E_{xm_x}-E_{gm_g}\quad E_{m21}\equiv E_{m2}-E_{m1}\ (m=g,x) \tag{S9}$$

Corrections to the electronic Raman due to electron-vibration coupling are

$$M_g \int \frac{dE_{g1}}{2\pi} \int \frac{dE_{g2}}{2\pi} \int \frac{dE_{x1}}{2\pi} \int \frac{dE_{x2}}{2\pi}$$

$$\Bigg(2\pi\delta(\nu_{if} - E_{g21} - E_{x21})\, G_g^<(E_{g1}) G_g^>(E_{g2}) G_x^<(E_{x1}) G_x^>(E_{x2}) \tag{S10a}$$

$$\times 2\mathrm{Re}\Bigg[\binom{1+N_v}{N_v} \frac{[U^{(1)}_{i,gx}U^{(0)}_{gx,f}G_g^r(E_{g2}\mp\omega_v) + U^{(0)}_{i,gx}U^{(1)}_{gx,f}G_g^a(E_{g1}\mp\omega_v)]U^{(0)}_{f,gx}U^{(0)}_{gx,i}}{(\nu_i - E_{x2g1} + i\delta)(\nu_i - E_{x2g1} \mp \omega_v - i\delta)}$$

$$+ N_v \frac{[U^{(0)}_{i,gx}U^{(1)}_{gx,f}G_g^r(E_{g2}\mp\omega_v) + U^{(1)}_{i,gx}U^{(0)}_{gx,f}G_g^a(E_{g1}\mp\omega_v)]U^{(0)}_{f,gx}U^{(0)}_{gx,i}}{|\nu_i - E_{x2g1} + i\delta|^2}$$

$$- i\int \frac{dE_3}{2\pi} \frac{G_g^<(E_{g3})U^{(0)}_{f,gx}U^{(0)}_{gx,i}}{\nu_i - E_{x2g1} + i\delta} \Bigg(\frac{U^{(1)}_{i,gx}U^{(0)}_{gx,f}[F(E_{g2},E_{g3}) - F(E_{g2},E_{g1})]}{\nu_i - E_{x2g1} - E_{g2g3} - i\delta}$$

$$+ \frac{U^{(0)}_{i,gx}U^{(1)}_{gx,f}[F(E_{g3},E_{g1}) - F(E_{g2},E_{g1})]}{\nu_i - E_{x2g3} - i\delta} \Bigg)$$

$$+ \frac{[U^{(1)}_{i,gx}U^{(0)}_{gx,f}\Phi(E_{g1}) + U^{(0)}_{i,gx}U^{(1)}_{gx,f}\Phi^*(E_{g2})]U^{(0)}_{f,gx}U^{(0)}_{gx,i}}{|\nu_i - E_{x2g1} + i\delta|^2} \Bigg]$$

$$- 2\pi\delta(\nu_{if} - E_{x21})\, G_g^<(E_{g1}) G_g^<(E_{g2}) G_x^<(E_{x1}) G_x^>(E_{x2}) \tag{S10b}$$

$$\times 2\mathrm{Re}\Bigg[\binom{1+N_v}{N_v} \frac{[U^{(1)}_{i,gx}U^{(0)}_{gx,f}G_g^r(E_{g2}\mp\omega_v) + U^{(0)}_{i,gx}U^{(1)}_{gx,f}G_g^a(E_{g2}\mp\omega_v)]U^{(0)}_{f,gx}U^{(0)}_{gx,i}}{(\nu_i - E_{x2g1} + i\delta)(\nu_i - E_{x2g2} \mp \omega_v - i\delta)}$$

$$+ N_v \frac{[U^{(0)}_{i,gx}U^{(1)}_{gx,f}G_g^r(E_{g2}\mp\omega_v) + U^{(1)}_{i,gx}U^{(0)}_{gx,f}G_g^a(E_{g2}\mp\omega_v)]U^{(0)}_{f,gx}U^{(0)}_{gx,i}}{(\nu_i - E_{x2g1} + i\delta)(\nu_i - E_{x2g2} - i\delta)}$$

$$+ \frac{[U^{(1)}_{i,gx}U^{(0)}_{gx,f}\Phi(E_{g2}) + U^{(0)}_{i,gx}U^{(1)}_{gx,f}\Phi^*(E_{g2})]U^{(0)}_{f,gx}U^{(0)}_{gx,i}}{(\nu_i - E_{x2g1} + i\delta)(\nu_i - E_{x2g2} - i\delta)} \Bigg]$$

$$- 2\pi\delta(\nu_{if} - E_{g21})\, G_g^<(E_{g1}) G_g^>(E_{g2}) G_x^>(E_{x1}) G_x^>(E_{x2})\, 2\mathrm{Re}\Bigg[\binom{1+N_v}{N_v} \tag{S10c}$$

$$\times \Bigg(\frac{U^{(1)}_{i,gx}U^{(0)}_{gx,f}G_g^r(E_{g2}\mp\omega_v)}{\nu_i - E_{x1g1} + i\delta} + \frac{U^{(0)}_{i,gx}U^{(1)}_{gx,f}G_g^a(E_{g1}\mp\omega_v)}{\nu_i - E_{x1g2} + i\delta} \Bigg) \frac{U^{(0)}_{f,gx}U^{(0)}_{gx,i}}{\nu_i - E_{x2g1} \mp \omega_v - i\delta}$$

$$+ N_v \frac{U^{(0)}_{f,gx}U^{(0)}_{gx,i}}{\nu_i - E_{x2g1} + i\delta} \Bigg(\frac{U^{(0)}_{i,gx}U^{(1)}_{gx,f}G_g^r(E_{g2}\mp\omega_v)}{\nu_i - E_{x1g1} \mp \omega_v - i\delta} + \frac{U^{(1)}_{i,gx}U^{(0)}_{gx,f}G_g^a(E_{g1}\mp\omega_v)}{\nu_i - E_{x1g1} - i\delta} \Bigg)$$

$$- i\int \frac{dE_3}{2\pi} \frac{G_g^<(E_{g3})U^{(0)}_{f,gx}U^{(0)}_{gx,i}}{\nu_i - E_{x1g1} + i\delta} \Bigg(\frac{U^{(1)}_{i,gx}U^{(0)}_{gx,f}[F(E_{g2},E_{g3}) - F(E_{g2},E_{g1})]}{\nu_i - E_{x2g1} - E_{g2g3} - i\delta}$$

$$+ \frac{U^{(0)}_{i,gx}U^{(1)}_{gx,f}[F(E_{g3},E_{g1}) - F(E_{g2},E_{g1})]}{\nu_i - E_{x2g3} - i\delta} \Bigg)$$

$$+ \frac{[U^{(1)}_{i,gx}U^{(0)}_{gx,f}\Phi(E_{g1}) + U^{(0)}_{i,gx}U^{(1)}_{gx,f}\Phi^*(E_{g2})]U^{(0)}_{f,gx}U^{(0)}_{gx,i}}{(\nu_i - E_{x1g1} + i\delta)(\nu_i - E_{x2g1} - i\delta)} \Bigg]$$

$$+ 2\pi\delta(\nu_i - \nu_f)\, G_g^<(E_{g1}) G_g^<(E_{g2}) G_x^>(E_{x1}) G_x^>(E_{x2}) \tag{S10d}$$

$$\times 2\mathrm{Re}\Bigg[\binom{1+N_v}{N_v} \frac{[U^{(1)}_{i,gx}U^{(0)}_{gx,f}G_g^r(E_{g2}\mp\omega_v) + U^{(0)}_{i,gx}U^{(1)}_{gx,f}G_g^a(E_{g2}\mp\omega_v)]U^{(0)}_{f,gx}U^{(0)}_{gx,i}}{(\nu_i - E_{x1g1} + i\delta)(\nu_i - E_{x2g2} \mp \omega_v - i\delta)}$$

$$+ N_v \frac{[U^{(0)}_{i,gx}U^{(1)}_{gx,f}G_g^r(E_{g2}\mp\omega_v) + U^{(1)}_{i,gx}U^{(0)}_{gx,f}G_g^a(E_{g2}\mp\omega_v)]U^{(0)}_{f,gx}U^{(0)}_{gx,i}}{(\nu_i - E_{x1g1} + i\delta)(\nu_i - E_{x2g2} - i\delta)}$$

$$+ \frac{[U^{(1)}_{i,gx}U^{(0)}_{gx,f}\Phi(E_{g2}) + U^{(0)}_{i,gx}U^{(1)}_{gx,f}\Phi^*(E_{g2})]U^{(0)}_{f,gx}U^{(0)}_{gx,i}}{(\nu_i - E_{x1g1} + i\delta)(\nu_i - E_{x2g2} - i\delta)} \Bigg] \Bigg)$$

where upper (lower) row and sign correspond to Stokes (anti-Stokes) scattering channel, repectively, and

$$F(E_1, E_2) \equiv \frac{1}{\omega_v - E_{21} + i\delta} + \frac{1}{\omega_v + E_{21} - i\delta} \tag{S11}$$

$$\Phi(E) \equiv i \int \frac{dE'}{2\pi} \left(\frac{G_g^>(E')}{E - E' - \omega_v - i\delta} - \frac{G_g^<(E')}{E - E' + \omega_v - i\delta} + \frac{2G_g^<(E')}{\omega_v} \right) \tag{S12}$$

At steady-state explicit expression for the vibrational Raman is

$$\int \frac{dE_{g1}}{2\pi} \int \frac{dE_{g2}}{2\pi} \int \frac{dE_{x1}}{2\pi} \int \frac{dE_{x2}}{2\pi} \begin{pmatrix} 1 + N_v \\ N_v \end{pmatrix}$$

$$\Bigg(2\pi\delta(\nu_{if} - E_{g21} - E_{x21} \mp \omega_v)\, G_g^<(E_{g1}) G_g^>(E_{g2}) G_x^<(E_{x1}) G_x^>(E_{x2}) \tag{S13a}$$

$$\times \Bigg[2\mathrm{Re} \frac{U_{i,gx}^{(0)} U_{gx,f}^{(1)} U_{f,gx}^{(0)} U_{gx,i}^{(1)}}{(\nu_i - E_{x2g1} + i\delta)(\nu_i - E_{x2g1} \mp \omega_v - i\delta)}$$

$$+ \frac{U_{i,gx}^{(1)} U_{gx,f}^{(0)} U_{f,gx}^{(0)} U_{gx,i}^{(1)}}{|\nu_i - E_{x2g1} \mp \omega_v + i\delta|^2} + \frac{U_{i,gx}^{(0)} U_{gx,f}^{(1)} U_{f,gx}^{(1)} U_{gx,i}^{(0)}}{|\nu_i - E_{x2g1} + i\delta|^2} \Bigg]$$

$$- 2\pi\delta(\nu_{if} - E_{x21} \mp \omega_v)\, G_g^<(E_{g1}) G_g^<(E_{g2}) G_x^<(E_{x1}) G_x^>(E_{x2}) \tag{S13b}$$

$$\times \Bigg[2\mathrm{Re} \frac{U_{i,gx}^{(0)} U_{gx,f}^{(1)} U_{f,gx}^{(0)} U_{gx,i}^{(1)}}{(\nu_i - E_{x2g2} + i\delta)(\nu_i - E_{x2g1} \mp \omega_v - i\delta)}$$

$$+ \frac{U_{i,gx}^{(1)} U_{gx,f}^{(0)} U_{f,gx}^{(0)} U_{gx,i}^{(1)}}{(\nu_i - E_{x2g2} \mp \omega_v + i\delta)(\nu_i - E_{x2g1} \mp \omega_v - i\delta)}$$

$$+ \frac{U_{i,gx}^{(0)} U_{gx,f}^{(1)} U_{f,gx}^{(1)} U_{gx,i}^{(0)}}{(\nu_i - E_{x2g2} + i\delta)(\nu_i - E_{x2g1} - i\delta)} \Bigg]$$

$$- 2\pi\delta(\nu_{if} - E_{g21} \mp \omega_v)\, G_g^<(E_{g1}) G_g^>(E_{g2}) G_x^>(E_{x1}) G_x^>(E_{x2}) \tag{S13c}$$

$$\times \Bigg[2\mathrm{Re} \frac{U_{i,gx}^{(0)} U_{gx,f}^{(1)} U_{f,gx}^{(0)} U_{gx,i}^{(1)}}{(\nu_i - E_{x1g1} + i\delta)(\nu_i - E_{x2g1} \mp \omega_v - i\delta}$$

$$+ \frac{U_{i,gx}^{(1)} U_{gx,f}^{(0)} U_{f,gx}^{(0)} U_{gx,i}^{(1)}}{(\nu_i - E_{x1g1} \mp \omega_v + i\delta)(\nu_i - E_{x2g1} \mp \omega_v - i\delta)}$$

$$+ \frac{U_{i,gx}^{(0)} U_{gx,f}^{(1)} U_{f,gx}^{(1)} U_{gx,i}^{(0)}}{(\nu_i - E_{x1g1} + i\delta)(\nu_i - E_{x2g1} - i\delta)} \Bigg]$$

$$+ 2\pi\delta(\nu_{if} \mp \omega_v)\, G_g^<(E_{g1}) G_g^<(E_{g2}) G_x^>(E_{x1}) G_x^>(E_{x2}) \tag{S13d}$$

$$\times \Bigg[2\mathrm{Re} \frac{U_{i,gx}^{(0)} U_{gx,f}^{(1)} U_{f,gx}^{(0)} U_{gx,i}^{(1)}}{(\nu_i - E_{x1g2} + i\delta)(\nu_i - E_{x2g1} \mp \omega_v - i\delta)}$$

$$+ \frac{U_{i,gx}^{(1)} U_{gx,f}^{(0)} U_{f,gx}^{(0)} U_{gx,i}^{(1)}}{(\nu_i - E_{x1g2} \mp \omega_v + i\delta)(\nu_i - E_{x2g1} \mp \omega_v - i\delta)}$$

$$+ \frac{U_{i,gx}^{(0)} U_{gx,f}^{(1)} U_{f,gx}^{(1)} U_{gx,i}^{(0)}}{(\nu_i - E_{x1g2} + i\delta)(\nu_i - E_{x2g1} - i\delta)} \Bigg] \Bigg)$$

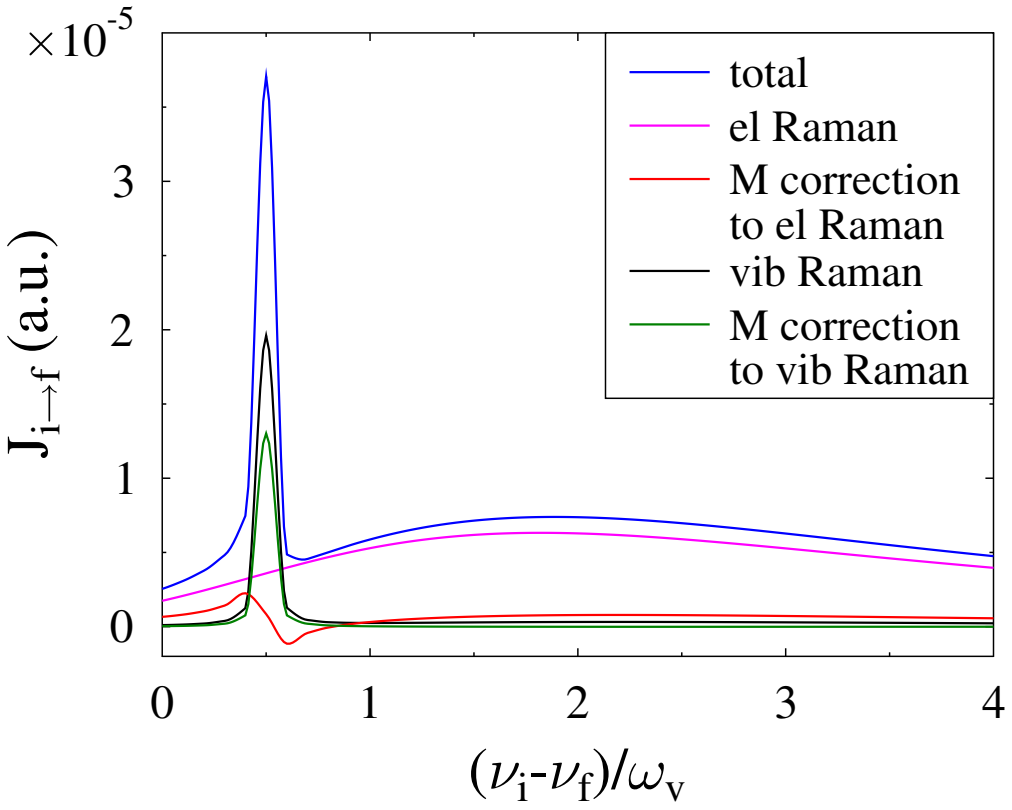

FIG. S6: (Color online) Intra-molecular Raman scattering (model A, see Fig. 3 of the paper). Shown are the total signal (blue line), electronic Raman (magenta) Eqs. (S8a)-(S8d) and its corrections due to electron-vibration interaction (red) Eqs. (S10a)-(S10d), as well as vibrational Raman (black) Eqs. (S13a)-(S13d) and its corrections due to electron-vibration interaction (green) Eqs. (S14a)-(S14d).

Corrections to the vibrational Raman due to electron-vibration coupling are

$$
\begin{aligned}
&M_g \int \frac{dE_{g1}}{2\pi} \int \frac{dE_{g2}}{2\pi} \int \frac{dE_{x1}}{2\pi} \int \frac{dE_{x2}}{2\pi} \begin{pmatrix} 1+N_v \\ N_v \end{pmatrix} \\
&\Bigg(2\pi\delta(\nu_{if} - E_{g21} - E_{x21} \mp \omega_v)\, G_g^<(E_{g1}) G_g^>(E_{g2}) G_x^<(E_{x1}) G_x^>(E_{x2}) \qquad \text{(S14a)} \\
&\times 2\mathrm{Re}\Bigg[\frac{G_g^r(E_{g1} \mp \omega_v)}{\nu_i - E_{x2g1} \mp \omega_v + i\delta} \left(\frac{U^{(0)}_{i,gx} U^{(0)}_{gx,f} U^{(0)}_{f,gx} U^{(1)}_{gx,i}}{\nu_i - E_{x2g1} \mp \omega_v - i\delta} + \frac{U^{(0)}_{i,gx} U^{(0)}_{gx,f} U^{(1)}_{f,gx} U^{(0)}_{gx,i}}{\nu_i - E_{x2g1} - i\delta} \right) \\
&\quad + \left(\frac{U^{(0)}_{i,gx} U^{(0)}_{gx,f} U^{(0)}_{f,gx} U^{(1)}_{gx,i}}{\nu_i - E_{x2g1} \mp \omega_v - i\delta} + \frac{U^{(0)}_{i,gx} U^{(0)}_{gx,f} U^{(1)}_{f,gx} U^{(0)}_{gx,i}}{\nu_i - E_{x2g1} - i\delta} \right) \frac{G_g^a(E_{g2} \pm \omega_v)}{\nu_i - E_{x2g1} + i\delta} \Bigg] \\
&- 2\pi\delta(\nu_{if} - E_{x21} \mp \omega_v)\, G_g^<(E_{g1}) G_g^<(E_{g2}) G_x^<(E_{x1}) G_x^>(E_{x2}) \qquad \text{(S14b)} \\
&\times 2\mathrm{Re}\Bigg[\frac{G_g^r(E_{g1} \mp \omega_v)}{\nu_i - E_{x2g1} \mp \omega_v + i\delta} \left(\frac{U^{(0)}_{i,gx} U^{(0)}_{gx,f} U^{(0)}_{f,gx} U^{(1)}_{gx,i}}{\nu_i - E_{x2g2} \mp \omega_v - i\delta} + \frac{U^{(0)}_{i,gx} U^{(0)}_{gx,f} U^{(1)}_{f,gx} U^{(0)}_{gx,i}}{\nu_i - E_{x2g2} - i\delta} \right) \\
&\quad + \left(\frac{U^{(0)}_{i,gx} U^{(0)}_{gx,f} U^{(0)}_{f,gx} U^{(1)}_{gx,i}}{\nu_i - E_{x2g1} \mp \omega_v - i\delta} + \frac{U^{(0)}_{i,gx} U^{(0)}_{gx,f} U^{(1)}_{f,gx} U^{(0)}_{gx,i}}{\nu_i - E_{x2g1} - i\delta} \right) \frac{G_g^a(E_{g2} \pm \omega_v)}{\nu_i - E_{x2g2} + i\delta} \Bigg] \\
&- 2\pi\delta(\nu_{if} - E_{g21} \mp \omega_v)\, G_g^<(E_{g1}) G_g^>(E_{g2}) G_x^>(E_{x1}) G_x^>(E_{x2}) \qquad \text{(S14c)} \\
&\times 2\mathrm{Re}\Bigg[\frac{G_g^r(E_{g1} \mp \omega_v)}{\nu_i - E_{x2g1} \mp \omega_v + i\delta} \left(\frac{U^{(0)}_{i,gx} U^{(0)}_{gx,f} U^{(0)}_{f,gx} U^{(1)}_{gx,i}}{\nu_i - E_{x1g1} \mp \omega_v - i\delta} + \frac{U^{(0)}_{i,gx} U^{(0)}_{gx,f} U^{(1)}_{f,gx} U^{(0)}_{gx,i}}{\nu_i - E_{x1g1} - i\delta} \right) \\
&\quad + \left(\frac{U^{(0)}_{i,gx} U^{(0)}_{gx,f} U^{(0)}_{f,gx} U^{(1)}_{gx,i}}{\nu_i - E_{x2g1} \mp \omega_v - i\delta} + \frac{U^{(0)}_{i,gx} U^{(0)}_{gx,f} U^{(1)}_{f,gx} U^{(0)}_{gx,i}}{\nu_i - E_{x2g1} - i\delta} \right) \frac{G_g^a(E_{g2} \pm \omega_v)}{\nu_i - E_{x1g1} + i\delta} \Bigg] \\
&+ 2\pi\delta(\nu_{if} \mp \omega_v)\, G_g^<(E_{g1}) G_g^<(E_{g2}) G_x^>(E_{x1}) G_x^>(E_{x2}) \qquad \text{(S14d)} \\
&\times 2\mathrm{Re}\Bigg[\frac{G_g^r(E_{g1} \mp \omega_v)}{\nu_i - E_{x2g1} \mp \omega_v + i\delta} \left(\frac{U^{(0)}_{i,gx} U^{(0)}_{gx,f} U^{(0)}_{f,gx} U^{(1)}_{gx,i}}{\nu_i - E_{x1g2} \mp \omega_v - i\delta} + \frac{U^{(0)}_{i,gx} U^{(0)}_{gx,f} U^{(1)}_{f,gx} U^{(0)}_{gx,i}}{\nu_i - E_{x1g2} - i\delta} \right) \\
&\quad + \left(\frac{U^{(0)}_{i,gx} U^{(0)}_{gx,f} U^{(0)}_{f,gx} U^{(1)}_{gx,i}}{\nu_i - E_{x2g1} \mp \omega_v - i\delta} + \frac{U^{(0)}_{i,gx} U^{(0)}_{gx,f} U^{(1)}_{f,gx} U^{(0)}_{gx,i}}{\nu_i - E_{x2g1} - i\delta} \right) \frac{G_g^a(E_{g2} \pm \omega_v)}{\nu_i - E_{x1g2} + i\delta} \Bigg] \Bigg)
\end{aligned}
$$

Similar to our previous considerations [34, 35] we are interested in Raman scattering only. Thus we drop Rayleigh contributions, Eqs. (S8d) and (S10d). The latter are sharply peaked peaked at $\nu_i = \nu_f$.

Results of numerical simulations presented in Fig. 3 of the paper show asymmetric scattering profile that becomes more pronounced at higher incident light intensity. Interference between the electronic and vibrational scattering pathway contributes to this asymmetry as seen in Fig. S6. This interference is associated with the corrections to the electronic Raman due to electron-vibration interaction, Eqs. (S10a)-(S10d) (the orange line showing the correction due to the coupling M to the electronic Raman scattering in Fig. S6). However, the dominant contribution to the line asymmetry is seen to be the Stokes nature of the electronic Raman scattering (purple line in Fig. S6) that dresses the vibrational peak on its high energy side.

Model B

Within the model B (see Fig. 2b of the paper) we focus on intra-molecular and charge transfer contributions, and disregard electron-vibration coupling (see Eq.(5) of the paper). Thus expressions (S2b)-(S2e), which are the source Fano-type interference in model A, do not contribute in this model. Within the model radiation field leads to optical excitation of either intra-molecular or charge transfer character. For each type of the excitations we separate vibrational and electronic degrees of freedom in the correlation function, disregard coherence between ground and excited states of the molecule, and perform integrals. A lengthy but straightforward derivations yield explicit expressions for electronic and vibrational Raman signal. The steady-state Raman flux from intial mode i to final mode f of the radiation field is

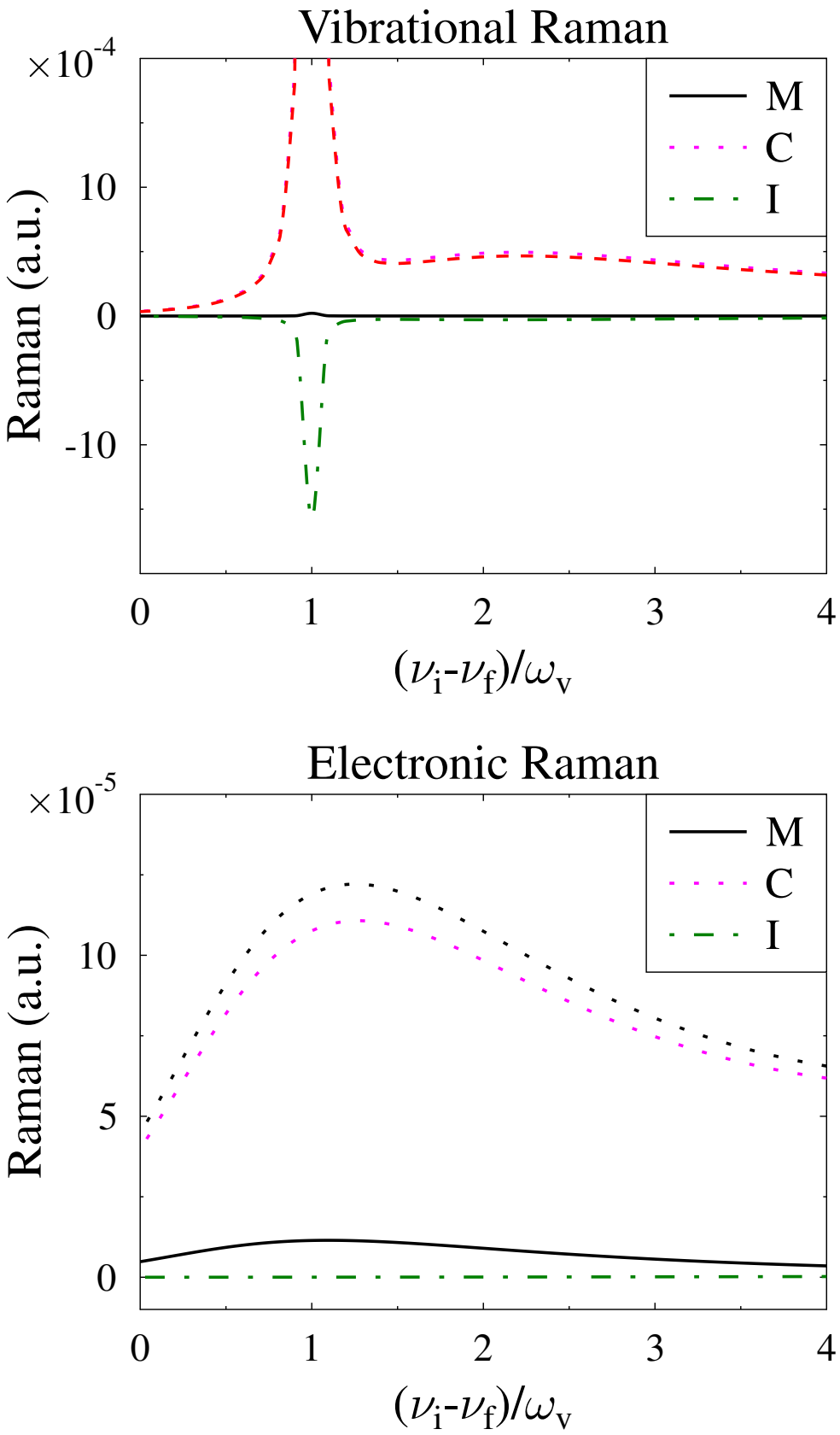

FIG. S7: (Color online) Vibrational (top) and electronic (bottom) Raman scattering (model B, see Fig. 5a of the paper). Shown are the total signals (dashed red line - top graph, dotted black line - bottom graph), as well as intra-molecular (solid black lines) and charge-transfer (dotted magenta lines), and their interferences (dash-dotted green lines).

Steady-state Raman flux from initial mode i to final mode f of the radiation field is

$$J_{i\to f} = \sum_{p=1}^{4} J_{i\to f}^{(p)} \tag{S15}$$

where

$$\begin{aligned}
J_{i\to f}^{(1)} = & \sum_{s=\{0,-,+\}} \int \frac{dE_g^{(1)}}{2\pi} \int \frac{dE_g^{(2)}}{2\pi} \int \frac{dE_x^{(1)}}{2\pi} \int \frac{dE_x^{(2)}}{2\pi} 2\pi\delta(\nu_{if} - E_g^{(21)} - E_x^{(21)} + s\omega_v) N_s \\
& \Bigg[G_g^<(E_g^{(1)}) G_g^>(E_g^{(2)}) G_x^<(E_x^{(1)}) G_x^>(E_x^{(2)}) \left| \frac{U_{fM}^{(1)} U_{Mi}^{(0)}}{\nu_i - E_x^{(2)} + E_g^{(1)} + i\delta} + \frac{U_{fM}^{(0)} U_{Mi}^{(1)}}{\nu_i - E_x^{(2)} + E_g^{(1)} + s\omega_v + i\delta} \right|^2 \\
& + \sum_{k_1,k_2} G_g^<(E_g^{(1)}) G_g^>(E_g^{(2)}) g_{k_1}^<(E_x^{(1)}) g_{k_2}^>(E_x^{(2)}) \left| \frac{U_{fC}^{(1)} U_{Ci}^{(0)}}{\nu_i - E_x^{(2)} + E_g^{(1)} + i\delta} + \frac{U_{fC}^{(0)} U_{Ci}^{(1)}}{\nu_i - E_x^{(2)} + E_g^{(1)} + s\omega_v + i\delta} \right|^2 \\
& + 2\mathrm{Re} \sum_{k_1,k_2} G_g^<(E_g^{(1)}) G_g^>(E_g^{(2)}) G_{k_1 x}^<(E_x^{(1)}) G_{x k_2}^>(E_x^{(2)}) \\
& \times \Bigg(\frac{U_{iM}^{(1)} U_{Mf}^{(0)} U_{fC}^{(1)} U_{Ci}^{(0)}}{(\nu_i - E_x^{(2)} + E_g^{(1)} + i\delta)(\nu_i - E_x^{(2)} + E_g^{(1)} + s\omega_v - i\delta)} + \frac{U_{iM}^{(1)} U_{Mf}^{(0)} U_{fC}^{(0)} U_{Ci}^{(1)}}{|\nu_i - E_x^{(2)} + E_g^{(1)} + s\omega_v + i\delta|^2} \\
& \quad + \frac{U_{iM}^{(0)} U_{Mf}^{(1)} U_{fC}^{(1)} U_{Ci}^{(0)}}{|\nu_i - E_x^{(2)} + E_g^{(1)} + i\delta|^2} + \frac{U_{iM}^{(0)} U_{Mf}^{(1)} U_{fC}^{(0)} U_{Ci}^{(1)}}{(\nu_i - E_x^{(2)} + E_g^{(1)} + s\omega_v + i\delta)(\nu_i - E_x^{(2)} + E_g^{(1)} - i\delta)} \Bigg) \Bigg]
\end{aligned} \tag{S16}$$

$$\begin{aligned}
J_{i\to f}^{(2)} = & -\sum_{s=\{0,-,+\}} \int \frac{dE_g^{(1)}}{2\pi} \int \frac{dE_g^{(2)}}{2\pi} \int \frac{dE_x^{(1)}}{2\pi} \int \frac{dE_x^{(2)}}{2\pi} \Bigg(2\pi\delta(\nu_{if} - E_x^{(21)} + s\omega_v) N_s \\
& \Bigg[G_g^<(E_g^{(1)}) G_g^<(E_g^{(2)}) G_x^<(E_x^{(1)}) G_x^>(E_x^{(2)}) \left| \frac{U_{fM}^{(1)} U_{Mi}^{(0)}}{\nu_i - E_x^{(2)} + E_g^{(1)} + i\delta} + \frac{U_{fM}^{(0)} U_{Mi}^{(1)}}{\nu_i - E_x^{(2)} + E_g^{(2)} + s\omega_v + i\delta} \right|^2 \\
& + \sum_{k_1,k_2} G_g^<(E_g^{(1)}) G_g^<(E_g^{(2)}) g_{k_1}^<(E_x^{(1)}) g_{k_2}^>(E_x^{(2)}) \left| \frac{U_{fC}^{(1)} U_{Ci}^{(0)}}{\nu_i - E_x^{(2)} + E_g^{(1)} + i\delta} + \frac{U_{fC}^{(0)} U_{Ci}^{(1)}}{\nu_i - E_x^{(2)} + E_g^{(2)} + s\omega_v + i\delta} \right|^2 \\
& + 2\mathrm{Re} \sum_{k_1,k_2} G_g^<(E_g^{(1)}) G_g^<(E_g^{(2)}) G_{k_1 x}^<(E_x^{(1)}) G_{x k_2}^>(E_x^{(2)}) \\
& \times \Bigg(\frac{U_{iM}^{(1)} U_{Mf}^{(0)} U_{fC}^{(1)} U_{Ci}^{(0)}}{(\nu_i - E_x^{(2)} + E_g^{(1)} + i\delta)(\nu_i - E_x^{(2)} + E_g^{(2)} + s\omega_v - i\delta)} \\
& \quad + \frac{U_{iM}^{(1)} U_{Mf}^{(0)} U_{fC}^{(0)} U_{Ci}^{(1)}}{(\nu_i - E_x^{(2)} + E_g^{(1)} + s\omega_v + i\delta)(\nu_i - E_x^{(2)} + E_g^{(2)} + s\omega_v - i\delta)} \\
& \quad + \frac{U_{iM}^{(0)} U_{Mf}^{(1)} U_{fC}^{(1)} U_{Ci}^{(0)}}{(\nu_i - E_x^{(2)} + E_g^{(1)} + i\delta)(\nu_i - E_x^{(2)} + E_g^{(2)} - i\delta)} \\
& \quad + \frac{U_{iM}^{(0)} U_{Mf}^{(1)} U_{fC}^{(0)} U_{Ci}^{(1)}}{(\nu_i - E_x^{(2)} + E_g^{(2)} + s\omega_v + i\delta)(\nu_i - E_x^{(2)} + E_g^{(1)} - i\delta)} \Bigg) \Bigg]
\end{aligned} \tag{S17}$$

$$J^{(3)}_{i\to f} = -\sum_{s=\{0,-,+\}} \int \frac{dE^{(1)}_g}{2\pi} \int \frac{dE^{(2)}_g}{2\pi} \int \frac{dE^{(1)}_x}{2\pi} \int \frac{dE^{(2)}_x}{2\pi} \Bigg(2\pi\delta(\nu_{if} - E^{(21)}_g + s\omega_v) N_s \tag{S18}$$

$$\Bigg[G^<_g(E^{(1)}_g) G^>_g(E^{(2)}_g) G^>_x(E^{(1)}_x) G^>_x(E^{(2)}_x) \left| \frac{U^{(1)}_{fM} U^{(0)}_{Mi}}{\nu_i - E^{(1)}_x + E^{(1)}_g + i\delta} + \frac{U^{(0)}_{fM} U^{(1)}_{Mi}}{\nu_i - E^{(2)}_x + E^{(1)}_g + s\omega_v + i\delta} \right|^2$$

$$+ \sum_{k_1,k_2} G^<_g(E^{(1)}_g) G^>_g(E^{(2)}_g) g^>_{k_1}(E^{(1)}_x) g^>_{k_2}(E^{(2)}_x) \left| \frac{U^{(1)}_{fC} U^{(0)}_{Ci}}{\nu_i - E^{(1)}_x + E^{(1)}_g + i\delta} + \frac{U^{(0)}_{fC} U^{(1)}_{Ci}}{\nu_i - E^{(2)}_x + E^{(1)}_g + s\omega_v + i\delta} \right|^2$$

$$+ 2\mathrm{Re} \sum_k G^<_g(E^{(1)}_g) G^>_g(E^{(2)}_g) g^>_k(E^{(1)}_x) G^>_x(E^{(2)}_x)$$

$$\times \Bigg(\frac{U^{(1)}_{iM} U^{(0)}_{Mf} U^{(1)}_{fC} U^{(0)}_{Ci}}{(\nu_i - E^{(1)}_x + E^{(1)}_g + i\delta)(\nu_i - E^{(2)}_x + E^{(1)}_g + s\omega_v - i\delta)}$$

$$+ \frac{U^{(1)}_{iM} U^{(0)}_{Mf} U^{(0)}_{fC} U^{(1)}_{Ci}}{(\nu_i - E^{(1)}_x + E^{(1)}_g + s\omega_v + i\delta)(\nu_i - E^{(2)}_x + E^{(1)}_g + s\omega_v - i\delta)}$$

$$+ \frac{U^{(0)}_{iM} U^{(1)}_{Mf} U^{(1)}_{fC} U^{(0)}_{Ci}}{(\nu_i - E^{(1)}_x + E^{(1)}_g + i\delta)(\nu_i - E^{(2)}_x + E^{(1)}_g - i\delta)}$$

$$+ \frac{U^{(0)}_{iM} U^{(1)}_{Mf} U^{(0)}_{fC} U^{(1)}_{Ci}}{(\nu_i - E^{(1)}_x + E^{(1)}_g + s\omega_v + i\delta)(\nu_i - E^{(2)}_x + E^{(1)}_g - i\delta)} \Bigg) \Bigg]$$

$$J^{(4)}_{i\to f} = \sum_{s=\{-,+\}} \int \frac{dE^{(1)}_g}{2\pi} \int \frac{dE^{(2)}_g}{2\pi} \int \frac{dE^{(1)}_x}{2\pi} \int \frac{dE^{(2)}_x}{2\pi} \Bigg(2\pi\delta(\nu_{if} + s\omega_v) N_s \tag{S19}$$

$$\Bigg[G^<_g(E^{(1)}_g) G^<_g(E^{(2)}_g) G^>_x(E^{(1)}_x) G^>_x(E^{(2)}_x) \left| \frac{U^{(1)}_{fM} U^{(0)}_{Mi}}{\nu_i - E^{(1)}_x + E^{(2)}_g + i\delta} + \frac{U^{(0)}_{fM} U^{(1)}_{Mi}}{\nu_i - E^{(2)}_x + E^{(1)}_g + s\omega_v + i\delta} \right|^2$$

$$+ \sum_{k_1,k_2} G^<_g(E^{(1)}_g) G^>_g(E^{(2)}_g) g^>_{k_1}(E^{(1)}_x) g^>_{k_2}(E^{(2)}_x) \left| \frac{U^{(1)}_{fC} U^{(0)}_{Ci}}{\nu_i - E^{(1)}_x + E^{(2)}_g + i\delta} + \frac{U^{(0)}_{fC} U^{(1)}_{Ci}}{\nu_i - E^{(2)}_x + E^{(1)}_g + s\omega_v + i\delta} \right|^2$$

$$+ 2\mathrm{Re} \sum_k G^<_g(E^{(1)}_g) G^<_g(E^{(2)}_g) g^>_k(E^{(1)}_x) G^>_x(E^{(2)}_x)$$

$$\times \Bigg(\frac{U^{(1)}_{iM} U^{(0)}_{Mf} U^{(1)}_{fC} U^{(0)}_{Ci}}{(\nu_i - E^{(1)}_x + E^{(2)}_g + i\delta)(\nu_i - E^{(2)}_x + E^{(1)}_g + s\omega_v - i\delta)}$$

$$+ \frac{U^{(1)}_{iM} U^{(0)}_{Mf} U^{(0)}_{fC} U^{(1)}_{Ci}}{(\nu_i - E^{(1)}_x + E^{(2)}_g + s\omega_v + i\delta)(\nu_i - E^{(2)}_x + E^{(1)}_g + s\omega_v - i\delta)}$$

$$+ \frac{U^{(0)}_{iM} U^{(1)}_{Mf} U^{(1)}_{fC} U^{(0)}_{Ci}}{(\nu_i - E^{(1)}_x + E^{(2)}_g + i\delta)(\nu_i - E^{(2)}_x + E^{(1)}_g + i\delta)}$$

$$+ \frac{U^{(0)}_{iM} U^{(1)}_{Mf} U^{(0)}_{fC} U^{(1)}_{Ci}}{(\nu_i - E^{(1)}_x + E^{(2)}_g + s\omega_v + i\delta)(\nu_i - E^{(2)}_x + E^{(1)}_g - i\delta)} \Bigg) \Bigg]$$

Here $\nu_{if} \equiv \nu_i - \nu_f$, $E^{(21)}_g \equiv E^{(2)}_g - E^{(1)}_g$, $E^{(21)}_x \equiv E^{(2)}_x - E^{(1)}_x$, $G^{>(<)}_{g(x)}$ is greater (lesser) projection of the molecular Green function, $g^{>(<)}_k$ is greater (lesser) projection of Green function representing free electrons in nanoparticles

$$g_k(\tau,\tau') \equiv -i\langle T_c\, \hat{c}_k(\tau)\, \hat{c}^\dagger_k(\tau')\rangle, \tag{S20}$$

and $G_{kx}^{>(<)}$ and $G_{xk}^{>(<)}$ are greater (lesser) projections of the mixed (molecule-nanoparticle) Green functions

$$G_{kx}(\tau,\tau') \equiv -i\langle T_c\, \hat{c}_k(\tau)\, \hat{d}_x^\dagger(\tau')\rangle \tag{S21}$$

$$G_{xk}(\tau,\tau') \equiv -i\langle T_c\, \hat{d}_x(\tau)\, \hat{c}_k^\dagger(\tau')\rangle \tag{S22}$$

In Eqs. (S16)-(S19) sum over s ($= \{0,-,+\}$) corresponds to electronic ($s=0$) and Stokes ($s=-$) and anti-Stokes ($s=+$) vibrational contributions to the total Raman signal with

$$N_s = \begin{cases} 1 & s=0 \\ N_v+1 & s=- \\ N_v & s=+ \end{cases} \tag{S23}$$

(N_v is average population of the vibrational mode). Note that Eq. (S19) contributes to vibrational Raman only. Its electronic part contributes to Rayleigh scattering [34, 35], and is disregarded in our consideration. Each of four expressions (S16)-(S19) contains the pure contribution of channel M in their first row (these terms represent the equivalent of model A, but without the effect of the e-v coupling (5) and the pure contribution of channel C in their second row. The rest of these expressions correspond to interference between these channels. It should be emphasized that each of these contributions has in turn a vibrational Raman and electronic Raman components, characterized by the corresponding change (vibrational or electronic) in system state.

Numerical simulations presented in Fig. 5 of the paper show that this model is also capable of providing an asymmetric feature in the Stokes line. A closer examination of intra-molecular and charge-transfer contributions as well as their interference to vibrational and electronic Raman scattering (see Fig. S7) indicate that the Fano-like feature in the total signal is mostly due to charge transfer contribution to the vibrational Raman scattering. This contribution consists of multiple scattering paths from different electronic states in the contact and in this sense it is an interference feature. However, as in model A, the scattering lineshape asymmetry is dominated by the electronic Stokes sideband dressing the molecular vibrational line.

[1] M. Moskovits, Rev. Mod. Phys. **57**, 783 (1985).
[2] J. I. Gersten and A. Nitzan, Surface Science **158**, 165 (1985).
[3] J. I. Gersten, Plasmonics **2**, 65 (2007).
[4] J. I. Gersten, R. L. Birke, and J. R. Lombardi, Phys. Rev. Lett. **43**, 147 (1979).
[5] A. Otto, I. Mrozek, H. Grabhorn, and W. Akemann, Journal of Physics: Condensed Matter **4**, 1143 (1992).
[6] A. Otto and M. Futamata, *Surface-Enhanced Raman Scattering: Physics and Applications* (Springer, 2006), vol. 103, chap. Electronic Mechanism of SERS, pp. 143–182.
[7] S. M. Morton, D. W. Silverstein, and L. Jensen, Chemical Reviews **111**, 3962 (2011).
[8] S. W. Wu, G. V. Nazin, and W. Ho, Phys. Rev. B **77**, 205430 (2008).
[9] Z. Ioffe, T. Shamai, A. Ophir, G. Noy, I. Yutsis, K. Kfir, O. Cheshnovsky, and Y. Selzer, Nature Nanotechnology **3**, 727 (2008).
[10] D. R. Ward, N. J. Halas, J. W. Ciszek, J. M. Tour, Y. Wu, P. Nordlander, and D. Natelson, Nano Lett. **8**, 919 (2008).
[11] Z. Liu, S.-Y. Ding, Z.-B. Chen, X. Wang, J.-H. Tian, J. R. Anema, X.-S. Zhou, D.-Y. Wu, B.-W. Mao, X. Xu, et al., Nat Commun **2**, 305 (2011).
[12] T. Shamai and Y. Selzer, Chem. Soc. Rev. **40**, 2293 (2011).
[13] D. R. Ward, D. A. Corley, J. M. Tour, and D. Natelson, Nature Nanotechnology **6**, 33 (2011).
[14] T. Konishi, M. Kiguchi, M. Takase, F. Nagasawa, H. Nabika, K. Ikeda, K. Uosaki, K. Ueno, H. Misawa, and K. Murakoshi, Journal of the American Chemical Society **135**, 1009 (2013).
[15] D. Natelson, Y. Li, and J. B. Herzog, Phys. Chem. Chem. Phys. **15**, 5262 (2013).
[16] M. Galperin and A. Nitzan, Phys. Chem. Chem. Phys. **14**, 9421 (2012).
[17] M. Galperin, M. A. Ratner, and A. Nitzan, Nano Lett. **9**, 758 (2009).
[18] M. Galperin, M. A. Ratner, and A. Nitzan, J. Chem. Phys. **130**, 144109 (2009).
[19] T.-H. Park and M. Galperin, Europhys. Lett. **95**, 27001 (2011).
[20] T.-H. Park and M. Galperin, Phys. Rev. B **84**, 075447 (2011).
[21] F. Mirjani, J. M. Thijssen, and M. A. Ratner, The Journal of Physical Chemistry C **116**, 23120 (2012).
[22] M. Oren, M. Galperin, and A. Nitzan, Phys. Rev. B **85**, 115435 (2012).
[23] T.-H. Park and M. Galperin, Phys. Scr. T **151**, 014038 (2012).
[24] K. Kaasbjerg, T. Novotný, and A. Nitzan, Phys. Rev. B **88**, 201405 (2013).
[25] A. J. White, S. Tretiak, and M. Galperin, Nano Letters **14**, 699 (2014).
[26] E. Burstein, Y. Chen, C. Chen, S. Lundquist, and E. Tosatti, Solid State Communications **29**, 567 (1979).
[27] W. Akemann and A. Otto, Surface Science **307-309, Part B**, 1071 (1994).

[28] T. Itoh, V. Biju, M. Ishikawa, Y. Kikkawa, K. Hashimoto, A. Ikehata, and Y. Ozaki, The Journal of Chemical Physics **124**, 134708 (2006).
[29] S. Marhaba, G. Bachelier, C. Bonnet, M. Broyer, E. Cottancin, N. Grillet, J. Lerm, J.-L. Vialle, and M. Pellarin, The Journal of Physical Chemistry C **113**, 4349 (2009).
[30] S. Yampolsky, D. A. Fishman, S. Dey, E. Hulkko, M. Banik, E. O. Potma, and V. A. Apkarian, Nat. Photon. **8**, 650 (2014).
[31] S. D. Ganichev, E. Ziemann, T. Gleim, W. Prettl, I. N. Yassievich, V. I. Perel, I. Wilke, and E. E. Haller, Phys. Rev. Lett. **80**, 2409 (1998).
[32] D. R. Ward, F. Huser, F. Pauly, J. C. Cuevas, and D. Natelson, Nature Nano **5**, 732 (2010).
[33] M. Vadai, N. Nachman, M. Ben-Zion, M. Brkle, F. Pauly, J. C. Cuevas, and Y. Selzer, The Journal of Physical Chemistry Letters **4**, 2811 (2013).
[34] M. Galperin and A. Nitzan, J. Phys. Chem. Lett. **2**, 2110 (2011).
[35] M. Galperin and A. Nitzan, Phys. Rev. B **84**, 195325 (2011).
[36] M. Banik, P. Z. El-Khoury, A. Nag, A. Rodriguez-Perez, N. Guarrottxena, G. C. Bazan, and V. A. Apkarian, ACS Nano **6**, 10343 (2012).
[37] A. Alù and N. Engheta, Phys. Rev. B **78**, 195111 (2008).
[38] J. T. Hugall and J. J. Baumberg, Nano Lett. **15**, 2600 (2015).
[39] M. Banik, Ph.D. thesis, UC Irvine, UC Irvine (2014).
[40] M. Galperin, M. A. Ratner, and A. Nitzan, The Journal of Chemical Physics **142**, 137101 (2015).
[41] M. Galperin, M. A. Ratner, and A. Nitzan, *On optical spectroscopy of molecular junctions*, arxiv:1503.03890 (2015), URL `http://arxiv.org/abs/1503.03890`.
[42] H. Haug and A.-P. Jauho, *Quantum Kinetics in Transport and Optics of Semiconductors*, vol. 123 (Springer, Berlin Heidelberg, 2008).
[43] We limit consideration to unbiased or weakly biased junctions, where only normal Raman scattering, where the initial electronic state is the ground state of the molecule, can take place.
[44] In particular, Eq. (S2a) leads to results discussed in our previous publications[34, 35] on electronic Raman scattering, while (S2g) - (S2j) are analogs of the terms considered in our treatment[17, 18] of (vibrational) resonant Raman scattering. Except that here we focus on the off-resonant scattering process.
[45] A closer look at the details of these corrections reveals that corrections to (S2b)-(S2c) from projections (e)-(h) of Fig. S5 and corrections to (S2d)-(S2e) from projections (a)-(d) of Fig. S5 represent renormalization of the electronic Raman signal due to e-v interaction. These terms dominate the resulting Fano resonance that is seen in the calculated Raman scattering at low incident lightintensity (inset to Fig. 3). Corrections to (S2b)-(S2c) from projections (a)-(d) of Fig. S5 and corrections to (S2d)-(S2e) from projections (e)-(h) of Fig. S5 lead to renormalization of the vibrational Raman scattering and are included as well in the calculations reported here.
[46] Eq. (S8) is the pure electronic Raman induced by the optical charge transfer molecule-metal coupling. A similar term with similar spectral characteristics corresponds to Raman scattering from the bare metal if the latter is structured enough (as opposed to a flat surface)
[47] In the calculation displayed in Fig 4 we have assumed that Γ^{opt} is dominated by the photo-induced charge transfer process.